



The Wolf–Rayet + Black Hole Binary NGC 300 X-1: What is the Mass of the Black Hole?

Breanna A. Binder¹ , Janelle M. Sy¹, Michael Eracleous² , Dimitris M. Christodoulou³ , Sayantan Bhattacharya³,
Rigel Cappallo³ , Silas Laycock³ , Paul P. Plucinsky⁴ , and Benjamin F. Williams⁵

¹ Department of Physics & Astronomy, California State Polytechnic University, 3801 W. Temple Ave, Pomona, CA 91768, USA; babinder@cpp.edu

² Department of Astronomy & Astrophysics and Institute for Gravitation and the Cosmos, The Pennsylvania State University, 525 Davey Lab, University Park, PA 16802, USA

³ Lowell Center for Space Science and Technology, University of Massachusetts Lowell, 600 Suffolk Street, Lowell, MA 01854, USA

⁴ Harvard-Smithsonian Center for Astrophysics, 60 Garden Street, Cambridge, MA 02138, USA

⁵ Department of Astronomy, University of Washington, Box 351580, Seattle, WA 98195, USA

Received 2021 January 11; revised 2021 February 9; accepted 2021 February 13; published 2021 March 29

Abstract

We present new X-ray and UV observations of the Wolf–Rayet + black hole (BH) binary system NGC 300 X-1 with the Chandra X-ray Observatory and the Hubble Space Telescope Cosmic Origins Spectrograph. When combined with archival X-ray observations, our X-ray and UV observations sample the entire binary orbit, providing clues to the system geometry and interaction between the BH accretion disk and the donor star wind. We measure a binary orbital period of 32.7921 ± 0.0003 hr, in agreement with previous studies, and perform phase-resolved spectroscopy using the X-ray data. The X-ray light curve reveals a deep eclipse, consistent with inclination angles of $i = 60^\circ$ – 75° , and a pre-eclipse excess consistent with an accretion stream impacting the disk edge. We further measure radial velocity variations for several prominent far-UV spectral lines, most notably H II $\lambda 1640$ and C IV $\lambda 1550$. We find that the He II emission lines systematically lag the expected Wolf–Rayet star orbital motion by a phase difference of $\Delta\phi \sim 0.3$, while C IV $\lambda 1550$ matches the phase of the anticipated radial velocity curve of the Wolf–Rayet donor. We assume the C IV $\lambda 1550$ emission line follows a sinusoidal radial velocity curve (semi-amplitude = 250 km s^{-1}) and infer a BH mass of $17 \pm 4 M_\odot$. Our observations are consistent with the presence of a wind-Roche lobe overflow accretion disk, where an accretion stream forms from gravitationally focused wind material and impacts the edge of the BH accretion disk.

Unified Astronomy Thesaurus concepts: High-mass x-ray binary stars (733); X-ray binary stars (1811); Astrophysical black holes (98); Stellar mass black holes (1611); Wolf–Rayet stars (1806)

Supporting material: animation

1. Introduction

High mass X-ray binaries (HMXBs) are systems composed of a massive OB star and a neutron star or black hole (BH). Winds from the stellar companion are accreted onto the compact object, releasing copious amounts of X-ray radiation. A large fraction of the X-rays that are generated close to the compact object escape—making these systems detectable as bright X-ray sources, with X-ray luminosities of $L_X \sim 10^{36-39} \text{ erg s}^{-1}$, but a significant fraction of X-rays will interact with material in the immediate environment and be reprocessed before becoming accessible to X-ray telescopes. X-ray reprocessing is ubiquitous in systems with accreting compact objects (de Jong et al. 1996; Suleimanov et al. 2003; Gierliński et al. 2009); in HMXBs, the wind of the donor star provides a reservoir of material in which X-ray reprocessing can occur. Observations of X-ray reprocessing in HMXBs have yielded important constraints on mass accretion mechanisms, the geometry of accreting systems, and the distribution and ionization state of the stellar wind material (Day & Stevens 1993; Aftab et al. 2019).

In this paper we take a closer look at the X-ray and UV properties of the Wolf–Rayet (WR) + BH HMXB NGC 300 X-1 (hereafter X-1). The high X-ray luminosity of the system ($\sim 5 \times 10^{38} \text{ erg s}^{-1}$ in the 0.35–8 keV energy band; Binder et al. 2015, 2011) and high fractional spectral variability rms value of ~ 0.2 (Earnshaw & Roberts 2017) are typical of

accreting BHs in a very high/steep power-law state. Evidence of a soft thermal component in the X-ray spectrum has been interpreted as a possible signature of X-ray reprocessing by the photoionized stellar wind from the WR donor (Carpano et al. 2007).

Previous radial velocity (RV) measurements of the He II $\lambda 4686$ emission line indicated a BH mass (M_{BH}) of $\sim 20 M_\odot$ (Crowther et al. 2010a), making X-1 host to the second-heaviest known stellar mass BH in an XRB (after IC 10 X-1; Prestwich et al. 2007; Barnard et al. 2008; Silverman & Filippenko 2008; Laycock et al. 2015a, 2015b). However, subsequent Chandra (Binder et al. 2015) and XMM-Newton (Carpano et al. 2019) observations revealed a phase shift between the X-ray eclipse light curve and the He II $\lambda 4686$ RV curve, suggesting that this emission line does not actually trace the motion of the WR component and casting doubt on prior estimates of M_{BH} . A similar phase offset was first observed in Cyg X-3 (van Kerkwijk 1993) and interpreted as the result of strong X-ray irradiation of the stellar wind. A phase shift in the He II $\lambda 4686$ RV curve was similarly observed in IC 10 X-1 (Laycock et al. 2015a, 2015b), further calling into question the reliability of BH mass estimates derived from this emission line.

It has been suggested that the bright He II $\lambda 4686$ emission lines observed in these systems may instead be originating from the BH accretion disk or a region of the donor star’s dense stellar wind that is shadowed from X-ray irradiation from the

BH (Binder et al. 2015; Laycock et al. 2015a, 2015b; Carpano et al. 2019). Additionally, He II $\lambda 4686$ emission has been observed originating from hot spots on compact object accretion disks, where an accretion stream flowing from the donor star through the L1 point impacts the outer edge of the accretion disk (e.g., Marsh & Horne 1990; Marsh et al. 1990). Line-driven winds, such as those from WR stars and other hot stars (Lucy & Solomon 1970; Castor et al. 1975), are strongly affected by X-ray irradiation from a close accreting compact object (Hatchett & McCray 1977; Fransson & Fabian 1980). At typical X-1 luminosities (L_X of a few $\times 10^{38}$ erg s $^{-1}$), the WR wind is expected to be highly ionized (Blondin et al. 1991; Manousakis & Walter 2015), and at very close orbital separations (the orbital period of X-1 is ~ 33 hr; Carpano et al. 2007; Crowther et al. 2010a; Carpano et al. 2019) may disrupt the wind acceleration mechanism to such an extent that a photoionization “wake” is formed (Blondin et al. 1990; Blondin 1994; Krtićka et al. 2015). This interaction between the X-ray irradiation from the BH and the stellar wind from the WR is expected to imprint itself on UV and X-ray spectra of HMXBs (as observed in some Galactic HMXBs, including Vela X-1 and 4U 1700-37, Kaper et al. 1994; Schulz et al. 2002).

We have obtained a new X-ray observation from the Chandra/Advanced CCD Imaging Spectrometer (ACIS-I) instrument and four epochs of far-UV (FUV) spectroscopy with the Hubble Space Telescope’s Cosmic Origins Spectrograph (HST/COS) to investigate the geometry of the X-1 binary, the mass transfer and mass accretion mechanisms operating in the system, and to attempt to place more reliable constraints on the mass of the BH. WR stars are bright UV sources, with strong emission from H II $\lambda 1640$ and resonance lines that are not available in the optical spectra (such as C IV $\lambda 1550$) that can be directly compared to previous optical observations. However, even modest uncertainties in the binary orbital period (~ 10 s; Carpano et al. 2019) will lead to large errors in determining the orbital phases at which both the archival optical spectra and new UV observations were obtained, translating into unacceptably large errors on any BH mass estimate. We therefore obtained a new X-ray observation with Chandra taken nearly simultaneously with the HST observations. When combined with archival X-ray observations, our new observation extends the baseline of available X-ray observations to two decades. These new observations have allowed us to dramatically refine the orbital period measurement, calculate to high accuracy the orbital phases at which the UV and optical spectra were obtained, and estimate the mass of the X-1 BH.

The outline of this paper is as follows. In Section 2, we describe the new and archival observations utilized in this work, along with details of our observing strategy and data processing. In Section 3, we refine the ephemeris of the X-1 binary, and in Section 4, we analyze the X-ray spectra of X-1 as a function of binary orbital phase. We present an analysis of the FUV spectra as a function of orbital phase in Section 5. In Section 6, we derive new constraints on the X-1 binary parameters and present a physical model to interpret our observations (the updated BH mass estimate is discussed specifically in Section 6.1). We also discuss the assumptions and caveats to our results in that section. We conclude with a summary of our findings in Section 7. Throughout this work, we assume a distance to NGC 300 of 2.0 Mpc (derived from the

tip of the red giant branch magnitudes observed by the HST; Dalcanton et al. 2009). Assuming $H_0 = 70$ km s $^{-1}$ Mpc $^{-1}$, we estimate the galaxy’s bulk recessional velocity is ~ 141 km s $^{-1}$ and the corresponding redshift is $z = 0.00047$ (which broadly agrees with direct measurements; e.g., Lauberts & Valentijn 1989).

2. New and Archival Observations

NGC 300 has been previously observed with the Chandra/ACIS-I three times (Binder et al. 2015, 2011) and with XMM-Newton seven times, primarily for the purpose of studying the X-ray binary population of its host galaxy (Binder et al. 2012); two deep XMM-Newton observations were performed in concert with the Nuclear Spectroscopic Telescope Array specifically to study NGC 300 X-1, and serendipitously caught the neighboring pulsar-HMXB (the supernova “impostor” SN 2010da) in an ultraluminous state (after which the object became known as NGC 300 ULX-1 (Carpano et al. 2018; Walton et al. 2018; Koliopanos et al. 2019). To add to this archival data set, we have obtained new Chandra/ACIS-I observations of NGC 300 (observation ID 22375) and four coordinated observations with HST/COS (program 15999) to perform FUV spectroscopy of X-1 throughout its orbital cycle. Table 1 summarizes the relevant information for all observations (new and archival) utilized in this work, which we have reprocessed as described below.

2.1. Chandra Data Reduction

All Chandra data reduction was done in CIAO⁶ v4.12 (Fruscione et al. 2006) and reprocessed from `evtl` using `chandra_repro` and standard reduction procedures. Background light curves were extracted, but we found no evidence for strong background flares in any of the four observations. We created good time intervals (GTIs) using `lc_clean`. All event data were filtered on these GTIs and restricted to the 0.5–7 keV energy range. The total usable Chandra exposure time was 235.9 ks, with the effective exposure times for the individual observations listed in Table 1.

Exposure maps and exposure-corrected Chandra images were created using the CIAO task `fluximage`; we assumed spectral weights appropriate for a $\Gamma = 1.7$ power law absorbed by the average foreground column density in the direction of NGC 300 ($N_H = 10^{21}$ cm $^{-2}$; HIPI Collaboration et al. 2016). All observations were corrected to the solar system barycenter to account for differences in photon arrival times due to both Chandra’s and the Earth’s orbital motion using the task `axbary`. The point-source detection tool `wavdetect` was used to detect X-ray sources in all four observations; as the source with the highest X-ray flux in NGC 300 at the times of the Chandra exposures, X-1 was robustly detected in all four observations.

To extract light curves, we assumed a circular source region (5″ radius, chosen to enclose $\sim 90\%$ of the Chandra point-spread function (PSF)) centered on the `wavdetect` position of X-1. Circular annuli were used to define the background region, with an inner radius set to 6″. The outer radius was set such that the background region contained ~ 100 counts; in all observations, this corresponds to an outer radius of $\sim 20''$. No faint X-ray sources were detected within the background region

⁶ <http://cxc.harvard.edu/ciao>

Table 1
Observation Log

Observatory (1)	Instrument (2)	Observation Date (3)	Observation ID # (4)	Exposure Time (5)	New or Archival? (6)	Orbital Phase ^a (7)
XMM-Newton	EPIC pn	2000 Dec 27	0112800201	34.6	Archival	0.60–0.93
XMM-Newton	EPIC pn	2001 Jan 1	0112800101	27.5	Archival	0.46–0.63
XMM-Newton	EPIC pn	2005 May 22	0305860401	29.4	Archival	0.80–1.08
XMM-Newton	EPIC pn	2005 Nov 25	0305860301	29.3	Archival	0.73–1.02
XMM-Newton	EPIC pn	2010 May 28	0656780401	10.6	Archival	0.90–1.00
Chandra	ACIS-I	2010 Sep 24	12238	63.0 ks	Archival	0.64–1.18
Chandra	ACIS-I	2014 May 16	16028	64.2 ks	Archival	0.55–1.10
Chandra	ACIS-I	2014 Nov 17	16029	61.3 ks	Archival	0.76–1.29
XMM-Newton	EPIC pn	2016 Dec 17	0791010101	110.3 ks	Archival	0.00–1.00
XMM-Newton	EPIC pn	2016 Dec 19	0791010301	60.4 ks	Archival	0.06–0.73
Chandra	ACIS-I	2020 Apr 26	22375	47.4 ks	New	0.76–1.17
HST	COS/FUV	2020 Apr 27	15999–03	Two orbits	New	0.738–0.761
HST	COS/FUV	2020 Apr 27	15999–04	Two orbits	New	0.981–1.004
HST	COS/FUV	2020 Apr 29	15999–02	Two orbits	New	0.485–0.507
HST	COS/FUV	2020 Apr 30	15999–01	Two orbits	New	0.261–0.283

Note.^a See Section 3 for a discussion of the X-1 ephemeris and orbital phase calculations.

by `wavdetect` in any of the four Chandra observations. Background-subtracted light curves were then extracted using `dmextract` and binned to 2 ks. An image of the 0.5–7 keV source, using the new Chandra observation ObsID 22375, is shown in Figure 1, with the source and background light-curve extraction regions shown.

2.2. XMM-Newton Data Reduction

All XMM-Newton data reduction was performed with SAS 18.⁷ The raw `evtl` PN data were reprocessed with `epproc` and filtered at an energy range of 0.2–10 keV and `PATTERN` ≤ 4 . Background light curves were extracted using `evselect` and inspected for all observations, and GTIs were generated to reject observation times exhibiting background flaring events. The total usable GTI for all XMM-Newton observations was 302.1 ks, with the effective exposure times for the individual observations listed in Table 1.

We used the Chandra position to define the source and background extraction regions in the XMM-Newton field. A circular region of radius 20'' was used for the source region. Due to the brightness of nearby ($\sim 1'$) NGC 300 ULX-1 in two of the observations, we defined a circular background region positioned near X-1 on the same PN chip that was free from stray light contamination from ULX-1. We used a light-curve time resolution of 100 s. The SAS tool `epiclcorr` was used to correct the light curves for bad pixels, PSF variation at the location of X-1, as well as dead time, and vignetting.

2.3. HST/COS FUV Spectroscopy

We successfully obtained eight orbits with HST/COS to observe NGC 300 X-1 at four different phases of the binary's orbit. Two observations were obtained ~ 8 hr apart on 2020 April 27, and the remaining two observations were obtained on 2020 April 29 and 30. We used the G140L grating with a central wavelength of 1280 Å in `TIME-TAG` mode. This configuration produces two spectral segments, covering

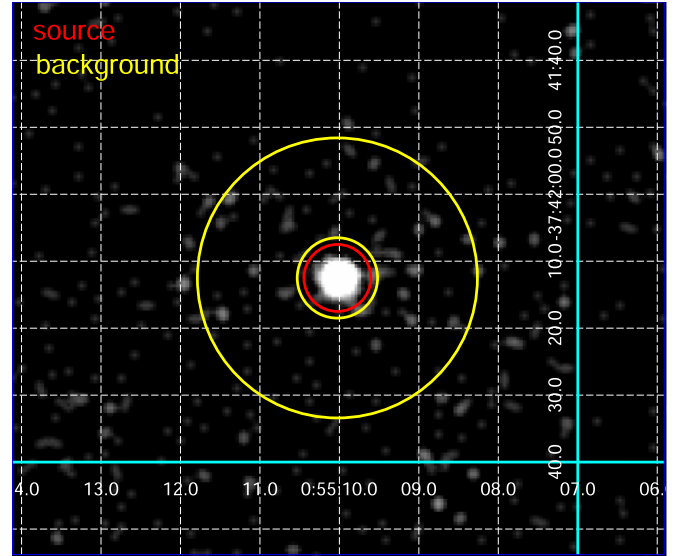


Figure 1. An X-ray image of X-1 from Chandra ObsID 22375. The red and yellow regions show the source and background regions, respectively, used to extract the Chandra light curves.

~ 915 – 2150 Å with a gap at 1193 – 1266 Å; our spectra therefore do not cover $\text{Ly}\alpha$. The spectral resolution is ~ 0.08 Å, and we estimate errors using Poisson statistics on the gross counts within each bin using the Gehrels approximation (Gehrels 1986).

The spectra of all four observations are shown in Figure 2. The spectral signal deteriorates toward the red and blue edges of the spectrum. Bright geocoronal airglow lines of O I at 1302 and 1305 Å are clearly seen, along with several fainter emission features intrinsic to the X-1 system. We discuss the FUV spectrum further in Section 5.

⁷ <https://www.cosmos.esa.int/web/xmm-newton/sas>

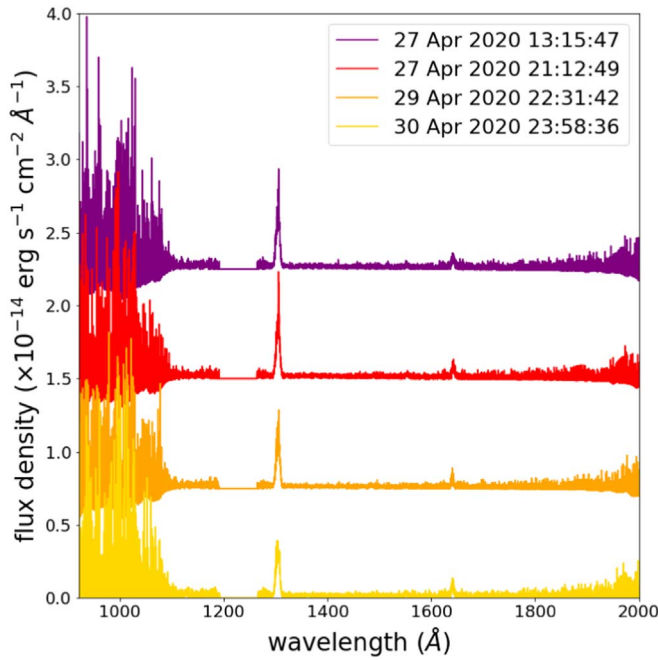


Figure 2. The HST/COS FUV spectra of NGC 300 X-1, color coded by observation date and start time. Observations have been given an arbitrary flux offset for clarity.

3. Refining the Orbital Period

In order to refine the orbital period measurement of the X-1 binary, we first aimed to phase fold all four Chandra observations with the deep XMM-Newton observations. The XMM-Newton observation obtained on 2016 December 19 captured the entire extent of the X-ray dip; we therefore used the light curve for this observation to identify, to the highest precision possible, the exact minimum of the dip, which we will define as the phase $\phi = 0.5$. As shown in Figure 3, an inverted Gaussian superimposed on a constant continuum count rate provided a good fit to the observed light curve, with the deepest part of the X-ray dip occurring at $t_d = 59,857,906$ s (mission seconds, corresponding to MJD 57742.00701).

The combined Chandra and XMM-Newton observations span a ~ 20 yr period, with only ~ 2 days separating the two deepest XMM-Newton observations. Given the long baseline of observations available for the system, maintaining phase connectivity would require knowing the orbital period to extremely high precision. The orbital period of X-1 was first determined to be ~ 32.8 hr from X-ray monitoring from the Neil Gehrels Swift Observatory (Carpano et al. 2007), and optical RV measurements of the He II $\lambda 4686$ emission line (Crowther et al. 2010a) were consistent with the X-ray orbital period. We therefore explored a set of trial periods ranging from 32.0–34.0 hr. The arrival times T of each Chandra and XMM-Newton event were transformed to orbital phase ϕ using the 2016 December 19 mid-dip time to define $\phi = 0.5$ (to avoid negative phases, we subtracted 100,000 cycles of the trial period, as was done in Laycock et al. (2015a):

$$\phi = \frac{(T - t_d - 100,000P)}{P}. \quad (1)$$

The time systems used by both Chandra and XMM-Newton share the same reference point (time elapsed since 1998.0 TT), so no additional time conversion between light curves is

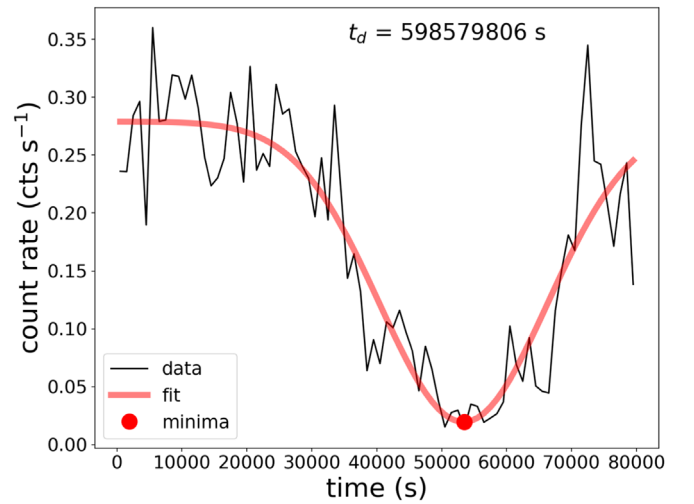


Figure 3. Finding the deepest part of the X-ray dip with XMM-Newton observation from 2016 December 19 (time 0 indicates the beginning of the observation). We defined the dip minimum as corresponding to phase $\phi = 0.5$.

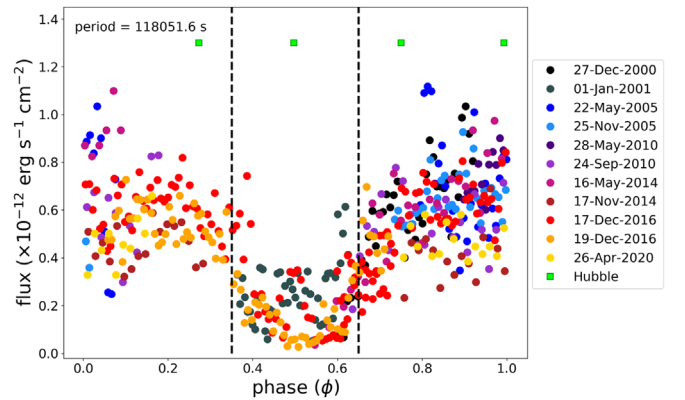


Figure 4. All Chandra and XMM-Newton light curves folded on the best orbital period, 32.7921 ± 0.0003 hr. The green squares indicate the phases at which the HST observations were obtained; the width of the squares indicates the spread in orbital phase due to the HST exposure time interval. The vertical-dashed lines show $\phi = 0.35$ and 0.65 , indicating the approximate extent of the X-ray eclipse. An animation of this figure is available. The animation shows folded light curves starting at 118,049.0 s to 118,054.8 s in 0.2 s increments. The real-time duration of the animation is 7 s.

(An animation of this figure is available.)

required between missions. We converted the count rates measured in the Chandra and XMM-Newton light curves to an (absorbed) 0.5–7 keV flux, assuming a basic power-law spectrum with $\Gamma = 1.7$ subject to an absorbing column of $N_H = 10^{21} \text{ cm}^{-2}$. A more detailed analysis of the evolution of the X-ray luminosity over the orbital period is discussed in Section 4. Folded light curves were initially generated in 1 s intervals and visually inspected. A period range of 118,049–118,055 s yielded relatively good phase connectivity; we therefore generated a new set of folded light curves within this range using 0.2 s increments and created a movie of the resulting phase-folded light curve (see the animation associated with Figure 4).

The best period is 32.7921 hr, as shown in Figure 4, in excellent agreement with previous studies (Carpano et al. 2019). We use our solution to determine the orbital phases at which the HST observations were taken; these are shown as green squares in Figure 4. A change in the orbital period

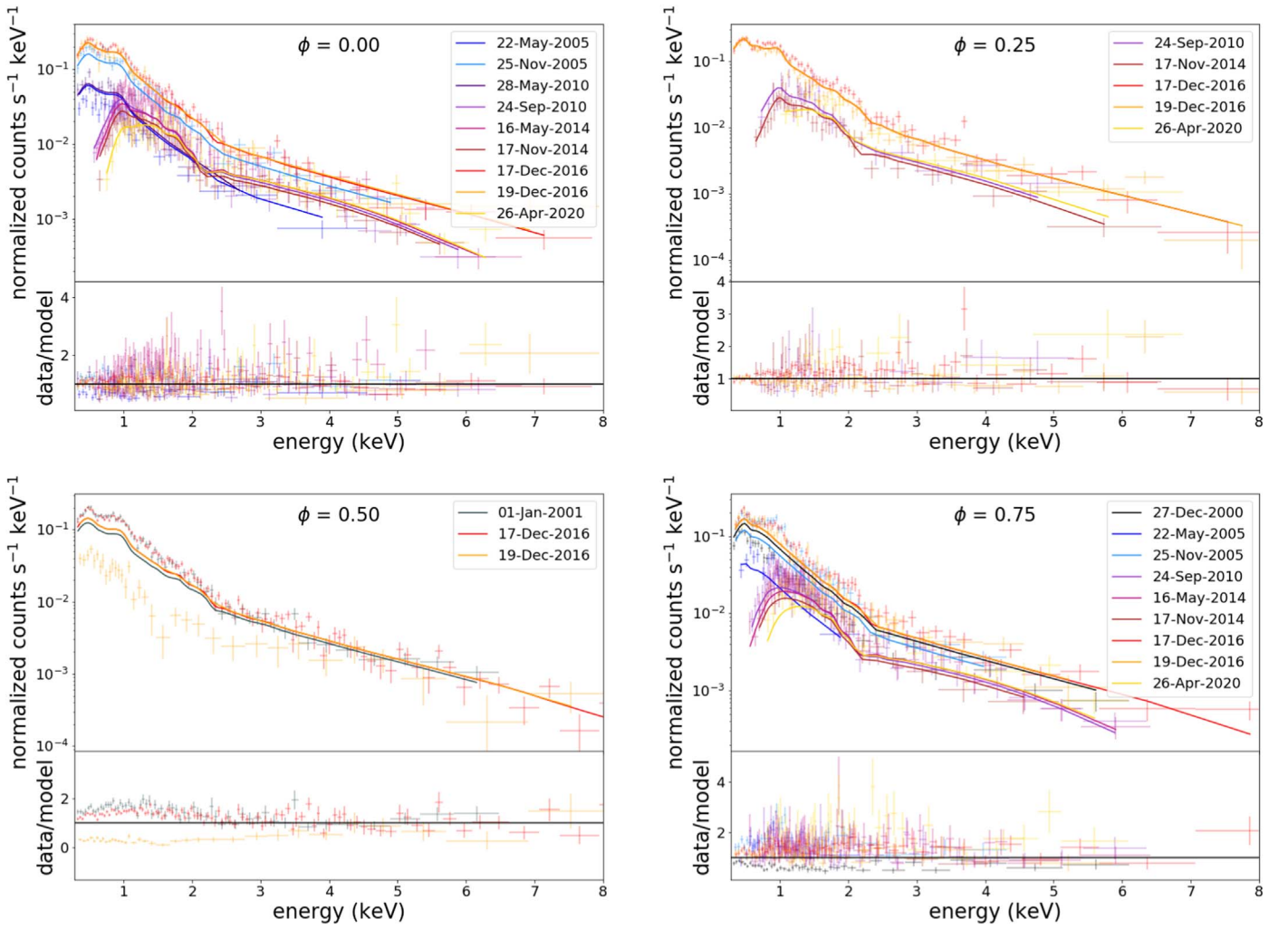


Figure 5. Phase-resolved X-ray spectroscopy with Chandra and XMM-Newton. All available spectra are fit simultaneously with all free parameters tied between observations. Colors are the same as in Figure 4.

of ± 1.2 s causes the dip structure between $\phi = 0.35$ and 0.65 to lose coherence; we therefore adopt 1.2 s (0.0003 hr) as the uncertainty in the orbital period.

4. Phase-resolved X-Ray Spectroscopy

As shown in Figure 4, the HST/COS observations were obtained at $\phi = 0.273, 0.497, 0.750$, and 0.993 , and multiple Chandra and XMM-Newton observations are available across the entire binary orbit. We therefore extracted four sets of X-ray spectra that correspond to the HST phases. We define these four phases as $\phi = 0.00$ (spanning phases 0.875 – 0.125), 0.25 (spanning phases 0.125 – 0.375 , corresponding to the X-ray dip ingress), 0.50 (corresponding to the X-ray dip at 0.375 – 0.625), and 0.75 (corresponding to the X-ray dip egress, spanning 0.625 – 0.875). All Chandra spectra were extracted using the CIAO task `specextract` in the energy range of 0.5 – 7 keV and binned to contain at least 10 counts per bin. Phase-resolved XMM-Newton PN spectra were extracted in the energy range 0.3 – 10 keV using `evselect` and binned to contain at least 25 counts per bin.

We simultaneously fitted all available X-ray spectra for in each phase bin with XSPEC v.12.9.1 (Arnaud 1996). All reported uncertainties correspond to the 90% confidence interval. Our spectral model consists of two thermal plasma

components (`mekal`) to model X-ray emission originating in the wind of the WR donor, a Comptonized continuum component with thermal seed photons (`comptt`) to represent the BH accretion disk, an absorbing column due to the Galaxy (`tbabs`, fixed at 10^{21} cm $^{-2}$; HI4PI Collaboration et al. 2016), and a partial covering absorbing column (`pcfabs`) to account for additional absorption of soft X-rays as the BH moves through the WR wind. The final XSPEC model is therefore `tbabs*pcfabs*(mekal+mekal+comptt)`, and the free parameters of the fit are the partial covering absorbing column density N_H , the partial covering fraction f_{cov} , the temperatures of the two thermal plasmas (kT_1 and kT_2), the “seed” temperature T_0 of the soft photons that interact with the Comptonizing plasma (which has a temperature of kT), and the optical depth τ of the Comptonizing plasma.

Initially, all free parameters in our model were free to vary, but they were tied to the same value for all of the simultaneously fitted spectra. Figure 5 shows the results of our simultaneous fitting as a function of orbital phase. Although the quality of the simultaneous fits was generally good ($\chi^2/\text{dof} < 2$) for observations at $\phi = 0.00$ and 0.25 , keeping parameters tied between observations yielded poor fits to the data at $\phi = 0.50$ and 0.75 . The best-fit parameters are summarized in Table 2. The quality of the spectral fits was

Table 2
Phase-resolved X-Ray Spectroscopy Best-fit Parameters

Parameter (1)	Orbital Phase ^a			
	0.00 (2)	0.25 (3)	0.50 (4)	0.75 (5)
N_H (10^{22} cm^{-2})	$4.1^{+1.6}_{-1.1}$	$2.1^{+0.7}_{-0.6}$	$3.1^{+0.8}_{-0.6}$	$5.1^{+2.2}_{-1.4}$
f_{cov}	$0.56^{+0.05}_{-0.06}$	0.57 ± 0.05	$0.70^{+0.08}_{-0.12}$	$0.66^{+0.08}_{-0.11}$
kT_1 (keV)	<0.2	...	<0.18	<0.25
kT_2 (keV)	0.8 ± 0.1	0.9 ± 0.1	$0.86^{+0.20}_{-0.11}$	$0.82^{+0.51}_{-0.29}$
Soft photon T_0 (keV)	<0.08	<0.07	<0.09	<0.08
Plasma kT (keV)	46 ± 19	51 ± 16	57 ± 13	50 ± 12
Optical depth τ	0.19 ± 0.02	0.14 ± 0.01	$0.12^{+0.02}_{-0.01}$	0.14 ± 0.01
χ^2/dof	987.8/493	353.9/200	4254.8/436	1873.5/436

Note.

^a The range of phases in each bin are described in Section 4 of the text. Uncertainties correspond to the 90% confidence interval.

significantly driven by the best-fit values of some parameters (such as N_H and the partial covering fraction f_{cov} , and possibly the optical depth of the Comptonizing plasma τ) while being insensitive to the values of other parameters.

We therefore refitted the X-ray spectra at each phase with the following parameters frozen: the two thermal plasma temperatures are fixed to $kT_1 = 0.1$ keV and $kT_2 = 0.8$ keV, and the soft photon and Comptonizing plasma temperatures are set to $T_0 = 0.1$ keV and $kT = 50$ keV, respectively. In this round of spectral fitting, we allow the partial covering absorbing column, covering fraction, and optical depth of the Comptonizing plasma (N_H , f_{cov} , and τ , respectively) to vary between observations within each phase bin. In addition, for each observation we measure the unabsorbed 0.3–10 keV luminosity (L_X), as well as the fluxes originating in the two thermal plasmas (which we refer to as the “thermal” component, likely associated with the WR star winds, as we discuss below) and the Comptonized component (which we call the “Compton” component, likely associated with the BH accretion disk).

Figure 6 shows the results of our second round of spectral fitting, and the best-fit parameters for individual observations as a function of orbital phase are summarized in Table 3. Some observations, when resolved into specific phase bins, did not contain a sufficient number of counts to directly constrain one or more of the free fit parameters; in these cases, we report upper or lower limits on the fit parameters as appropriate. We additionally report the average fit parameters (omitting observations with only limits on the fit parameters) as well as the percentage of the X-ray luminosity originating in the thermal component.

Figure 7 compares each of the three free fit parameters against the other two; we see no strong evidence for correlation between fit parameters. The average values of N_H , f_{cov} , and τ are largely consistent across orbital phase (see Figure 8). These results imply that bulk structure of the WR wind and BH accretion disk (or their orientation to our line of sight) are not changing significantly over the binary orbital phase.

Instead, it is the *unabsorbed* L_X that is changing at $\phi = 0.5$ when the BH accretion disk is partially eclipsed by the WR donor, along with the fraction of the L_X that originates in the thermal component (Figure 9). As expected, during the eclipse, L_X dips by a factor of ~ 1.3 and the thermal fraction increases

by a factor of ~ 2.6 . During non-eclipse phases, the Compton component of the X-ray spectrum accounts for $\sim 90\%$ of the overall value of L_X . The thermal fraction is additionally highest during the X-ray eclipse, suggesting that it is the Comptonized component—the BH accretion disk—that is being eclipsed, while X-rays intrinsic to the WR star and its winds remain largely unobscured (the Comptonizing component makes up only $\sim 70\%$ of the overall L_X at $\phi = 0.50$). There is additionally evidence of an enhancement in L_X at $\phi = 0.25$, although no corresponding change in the proportion of thermal X-rays is observed. The average unabsorbed 0.3–10 keV X-ray luminosity at phase $\phi = 0$ is $L_X = (8.6^{+0.5}_{-0.4}) \times 10^{38} \text{ erg s}^{-1}$; L_X at $\phi = 0.75$ is consistent with this value.

4.1. Discussion of Phase-resolved X-Ray Emission

With phase-resolved spectral fitting complete, we can now convert Chandra and XMM-Newton count rates to unabsorbed, 0.3–10 keV luminosities. We use the CIAO tool `modelflux` (along with appropriate response matrix and ancillary response files for each observation) to convert the observed count rates to flux values, using our physically motivated spectral model and the best-fit parameters derived for each observation as a function of orbital phase.

The reconstructed X-ray light curve, normalized such that the average L_X at $\phi = 0$ is 1, is shown in Figure 10. The binned light curve (black points) shows that the deepest portion of the eclipse ranges from $\phi = 0.4$ – 0.6 , and a clear L_X excess is observed at $\phi \sim 0.2$. We are able to fit the light curve with a double-Gaussian model: a deep, inverted Gaussian centered at $\phi \sim 0.5$ corresponding to the X-ray eclipse and a smaller Gaussian component describing the L_X excess centered at $\phi = 0.23$. We find a best-fit depth of the X-ray eclipse of -0.86 ± 0.03 (i.e., an $\sim 86\%$ decrease in L_X) and a best-fit amplitude of the X-ray excess of 0.30 ± 0.07 . Furthermore, there is evidence of asymmetry between the eclipse ingress and egress, with ingress occurring over $\Delta\phi \sim 0.15$ and egress spanning $\Delta\phi \sim 0.20$.

Pre-eclipse humps are commonly observed (in both the optical and UV) in other accreting compact object systems, such as cataclysmic variables (e.g., DW UMa; Stanishev et al. 2004; Hoard et al. 2010), and have been interpreted as bright spots in the compact object’s accretion disk resulting from the accretion stream from the L1 point impacting the edge of the disk. The soft X-ray photons from the shocked gas can photoionize the gas in the accretion flow and produce He II lines from the vicinity of the impact site. It is therefore reasonable to assume that the pre-eclipse hump observed in Figure 10 is the result of an accretion stream flowing through the L1 point and impacting the outer edge of the BH accretion disk. The asymmetry in the eclipse profile further supports this interpretation; in other XRBs (including the “twin” system IC 10 X-1; Laycock et al. 2015a) the eclipse profile asymmetry is explained as follows (Rutten et al. 1992). Due to conservation of angular momentum, the accretion stream that impacts the outer edge of the compact object accretion disk (generating the hot spot) lags the orbital motion of the compact object. As the compact object moves into the eclipse it is partially obscured by material in the accretion stream, while during eclipse egress the compact object leads the hot spot and the accretion stream. This leads to a small deficit in the X-ray luminosity during eclipse egress until the accretion stream and hot spot spin back into view of the observer. The temperatures and densities at

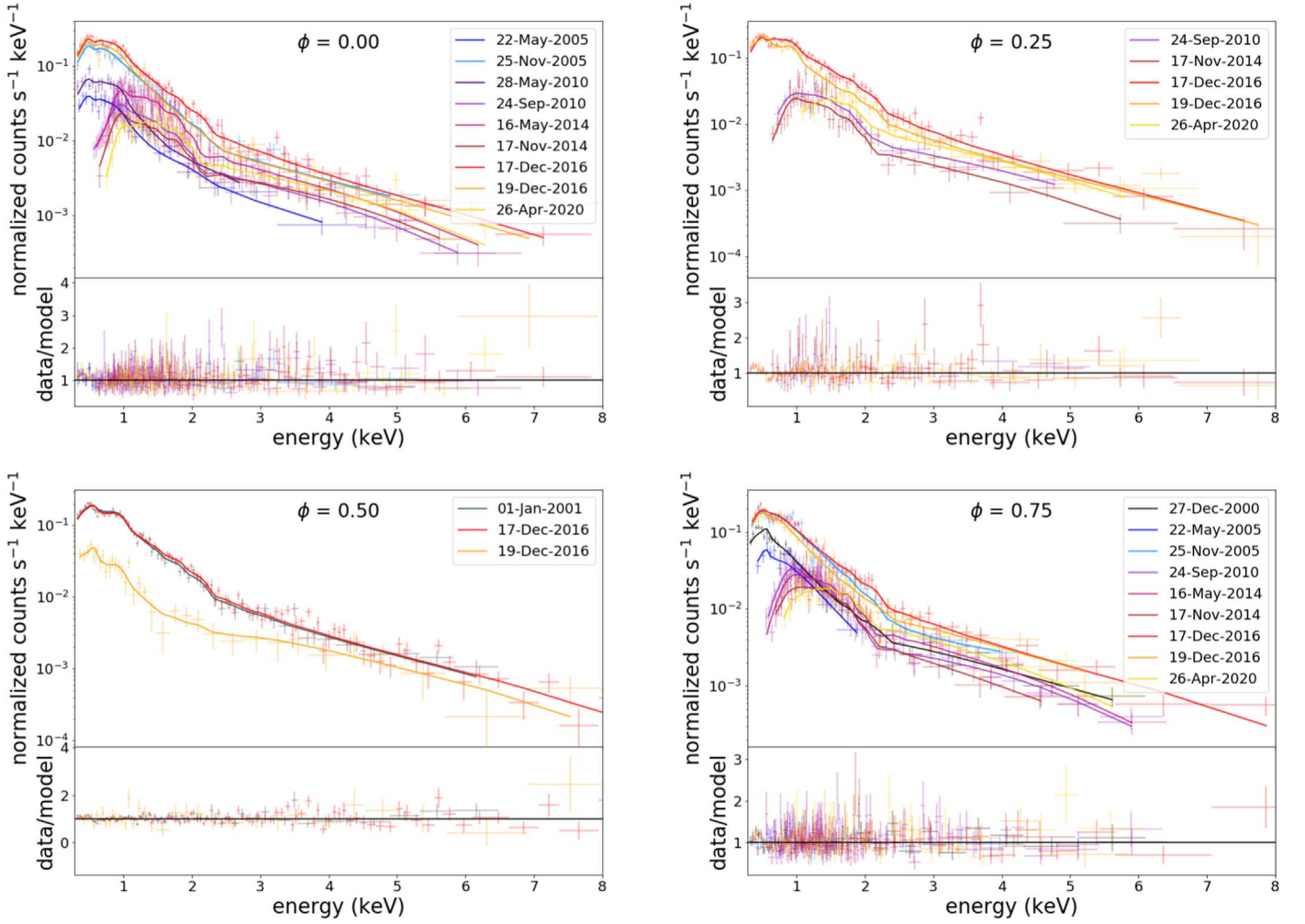


Figure 6. Phase-resolved X-ray spectroscopy with Chandra and XMM-Newton. All spectra were fit individually with the same spectral model, but the partial covering fraction f_{cov} and N_{H} and the Comptonizing plasma optical depth τ were allowed to vary between observations. All other fit parameters were fixed (see text for details). Colors are the same as in Figure 4.

these accretion stream impact sites are sufficient to produce strong He II emission lines (Montgomery 2012), providing a plausible explanation for the phase lag observed in the He II RV curve (Binder et al. 2015).

5. The UV Spectrum

WR stars exhibit strong, broad emission lines (Wolf & Rayet 1867) due to their dense and powerful stellar winds; the regions of the stellar wind that form these lines are geometrically extended, residing far from their parent stars, and the physical depth at which lines form within the wind is wavelength dependent (Crowther 2007). Because of the physical separation between the stellar radius and the line-formation region in the wind, the stellar temperatures T_* of WR stars are difficult to measure, and non-LTE atmospheric models are needed to interpret observed spectral features and infer physical properties of the star.

Generally, models of WR atmospheres are parameterized by the luminosity of the star (L_*) and the stellar temperature (T_*). Due to the geometrical extent of the winds compared to the stellar radius, it is common to define the inner boundary R_* as the radius at which the Rosseland optical depth is $\tau_{\text{R}} \sim 20$ (Todt et al. 2015); however, the optical continuum radiation

originates from the “photosphere” of the star (assumed to be where $\tau_{\text{R}} \sim 2/3$). In weak-lined, early-type WNs, such as the WR star in X-1 (identified as a WN5 subtype; Crowther et al. 2007, 2010a), R_* can be on the same order as $R_{2/3}$ (as in the case of HD 9974; Marchenko et al. 2004). Optical VLT/FORS2 spectroscopy obtained by Crowther et al. (2010a) has constrained $T_* \sim 65,000$ K (± 5000 K), $\log(L/L_\odot) \sim 5.92$, $\dot{M}_* \sim 5 \times 10^{-6} M_\odot \text{ yr}^{-1}$, and $v_\infty \sim 1300 \text{ km s}^{-1}$. These stellar parameters are consistent with a WN5 WR star with $M_* = 26_{-5}^{+7} M_\odot$, however a spectroscopic mass as low as $\sim 15 M_\odot$ is possible (and consistent with the masses of Galactic weak-lined WN5 stars; Hamann et al. 2006). The inferred stellar radius R_* is 7.2 or $4.8 R_\odot$ for the higher- and lower-mass estimates, respectively.

Due to their high temperatures, WR stars are also bright UV sources. Correlations between specific emission lines of singly ionized helium (He II) are of particular interest as He II is a recombination line in WR winds. Specifically, Conti & Morris (1990) observed an empirical correlation between the H II $\lambda 1640$ line ($n = 3 \rightarrow 2$, the singly ionized helium equivalent of H α) and He II $\lambda 4686$ ($n = 4 \rightarrow 3$, the equivalent of Pa α) lines in WN-type WR stars. The equivalent widths (EWs) and fluxes of the two lines are correlated for isolated WN stars; Leitherer

Table 3
Individual Observation Phase-resolved X-Ray Spectroscopy Best-fit Parameters

Observation Date (1)	N_{H} (10^{22} cm^{-2}) (2)	f_{cov} (3)	τ (4)	$\log F_{0.3-10}^{\text{thermal}}$ ($\text{erg s}^{-1} \text{ cm}^{-2}$) (5)	$\log F_{0.3-10}^{\text{Compton}}$ ($\text{erg s}^{-1} \text{ cm}^{-2}$) (6)	L_{X} (% thermal) ($\times 10^{38} \text{ erg s}^{-1}$) (7)	χ^2/dof (8)
Phase 0.00							
22 May 05	$4.3^{+2.1}_{-1.1}$	0.87 ± 0.02	0.06 ± 0.02	$-12.81^{+0.50}_{-0.20}$	-11.54 ± 0.05	$14.6^{+0.6}_{-0.2}$ (5.1)	20.8/23
25 Nov 05	$7.5^{+3.9}_{-2.9}$	$0.60^{+0.11}_{-0.20}$	0.12 ± 0.02	$-14.30^{+1.34}_{-0.74}$	$-11.70^{+0.12}_{-0.17}$	$9.8^{+0.9}_{-0.5}$ (0.2)	56.2/37
28 May 10	$6.9^{+4.5}_{-1.8}$	0.91 ± 0.02	$0.06^{+0.03}_{-0.02}$	$-12.16^{+0.38}_{-0.54}$	-11.17 ± 0.05	$35.9^{+1.1}_{-1.6}$ (9.2)	27.2/15
24 Sep 10	$2.9^{+3.2}_{-1.1}$	$0.57^{+0.11}_{-0.10}$	$0.16^{+0.08}_{-0.05}$	$-12.41^{+0.38}_{-1.08}$	$-12.00^{+2.70}_{-0.06}$	$6.7^{+0.2}_{-0.1}$ (27.8)	60.1/72
16 May 14	<0.34	>0.39	$0.26^{+0.06}_{-0.05}$	$-11.97^{+0.96}_{-1.78}$	$-12.07^{+0.11}_{-0.09}$	$9.5^{+0.8}_{-1.4}$ (54.0)	98.4/96
17 Nov 14	$3.7^{+2.5}_{-1.3}$	$0.63^{+0.20}_{-0.30}$	$0.20^{+0.30}_{-0.12}$	$-12.75^{+0.16}_{-0.26}$	$-11.97^{+0.40}_{-0.31}$	6.0 ± 0.2 (14.2)	43.7/55
17 Dec 16	$3.1^{+5.2}_{-3.3}$	$0.53^{+0.18}_{-0.26}$	0.12 ± 0.04	$-13.11^{+0.42}_{-0.71}$	$-11.83^{+0.17}_{-0.16}$	$7.6^{+0.3}_{-0.4}$ (4.9)	71.2/55
19 Dec 16	$6.8^{+4.1}_{-3.3}$	0.71 ± 0.02	0.09 ± 0.03	-13.03 ± 0.43	$-11.69^{+0.06}_{-0.07}$	10.3 ± 0.3 (4.3)	37.9/23
26 Apr 20	$1.6^{+5.0}_{-1.4}$	$0.29^{+0.36}_{-0.29}$	$0.35^{+0.32}_{-0.19}$	$-12.95^{+0.19}_{-0.58}$	$-12.18^{+0.27}_{-0.14}$	$3.8^{+0.1}_{-0.2}$ (14.1)	60.4/61
Average	$4.0^{+4.0}_{-1.7}$	$0.59^{+0.15}_{-0.18}$	$0.15^{+0.11}_{-0.07}$	$-12.96^{+0.42}_{-0.60}$	$-11.85^{+0.57}_{-0.14}$	$8.6^{+0.5}_{-0.4}$ (10.0)	...
Phase 0.25							
24 Sep 10	32.2 ± 13.9	<0.82	$0.31^{+0.35}_{-0.12}$	<-12.75	$-11.78^{+0.41}_{-0.47}$	8.1 ± 0.3 (<10.5)	21.5/16
17 Nov 14	$3.2^{+3.9}_{-3.0}$	<0.74	$0.19^{+0.24}_{-0.14}$	$-13.21^{+0.41}_{-1.50}$	$-12.07^{+0.52}_{-0.17}$	$4.4^{+0.2}_{-0.5}$ (6.7)	51.5/42
17 Dec 16	$1.4^{+0.6}_{-0.5}$	$0.65^{+0.18}_{-0.23}$	$0.09^{+0.06}_{-0.04}$	-12.85 ± 0.50	$-11.73^{+0.20}_{-0.21}$	10.0 ± 0.4 (6.8)	79.7/55
19 Dec 16	$3.1^{+1.8}_{-0.9}$	$0.76^{+0.11}_{-0.18}$	$0.07^{+0.04}_{-0.03}$	$-12.98^{+0.36}_{-0.64}$	$-11.66^{+0.22}_{-0.21}$	$11.2^{+0.4}_{-0.6}$ (4.5)	99.7/49
26 Apr 20	<3.3	<0.86	$0.19^{+0.14}_{-0.10}$	$-12.24^{+0.98}_{-4.07}$	$-11.89^{+1.29}_{-0.98}$	$9.2^{+1.2}_{-3.2}$ (29.9)	9.5/6
Average	$2.5^{+1.5}_{-1.6}$	$0.73^{+0.09}_{-0.44}$	$0.13^{+0.11}_{-0.07}$	$-12.76^{+0.56}_{-1.32}$	$-11.75^{+0.44}_{-0.38}$	$10.0^{+0.6}_{-1.1}$ (12.0)	...
Phase 0.50							
01 Jan 01	$2.9^{+2.5}_{-1.0}$	0.44 ± 0.07	0.16 ± 0.02	$-12.57^{+0.22}_{-0.30}$	-11.99 ± 0.02	6.2 ± 0.1 (20.8)	67.7/54
17 Dec 16	$1.7^{+1.0}_{-0.6}$	$0.49^{+0.15}_{-0.25}$	$0.17^{+0.06}_{-0.05}$	$-12.52^{+0.19}_{-0.20}$	-12.05 ± 0.13	5.8 ± 0.1 (24.9)	173.2/91
19 Dec 16	$6.4^{+3.0}_{-1.5}$	0.94 ± 0.02	$0.10^{+0.10}_{-0.04}$	$-12.08^{+0.19}_{-0.35}$	$-11.91^{+0.08}_{-0.06}$	$10.1^{+0.2}_{-0.3}$ (39.4)	24.2/27
Average	$3.3^{+1.8}_{-1.9}$	$0.62^{+0.10}_{-0.15}$	$0.15^{+0.07}_{-0.04}$	$-12.39^{+0.19}_{-0.26}$	$-12.00^{+0.10}_{-0.09}$	$7.2^{+0.1}_{-0.2}$ (28.4)	...
Phase 0.75							
27 Dec 00	$6.1^{+6.8}_{-2.4}$	$0.79^{+0.10}_{-0.20}$	$0.10^{+0.04}_{-0.03}$	$-12.39^{+0.13}_{-0.19}$	$-11.91^{+0.30}_{-0.29}$	7.9 ± 0.2 (24.7)	47.3/25
22 May 05	0.2 ± 0.1	>0.73	<0.09	$-12.09^{+0.16}_{-0.26}$	$-11.98^{+0.20}_{-0.21}$	$16.7^{+0.4}_{-0.5}$ (23.3)	9.5/5
25 Nov 05	>8.5	$0.71^{+0.26}_{-0.23}$	$0.12^{+0.03}_{-0.02}$	<-12.29	$-11.57^{+0.76}_{-0.48}$	$14.8^{+0.1}_{-1.2}$ (<16.6)	57.7/33
24 Sep 10	$7.1^{+5.4}_{-2.4}$	$0.69^{+0.16}_{-0.21}$	$0.11^{+0.12}_{-0.05}$	$-12.97^{+0.25}_{-0.65}$	$-11.77^{+0.35}_{-0.40}$	$8.8^{+0.3}_{-0.5}$ (5.8)	56.2/68
16 May 14	$2.0^{+2.0}_{-1.6}$	$0.33^{+0.22}_{-0.09}$	$0.21^{+0.16}_{-0.05}$	$-12.68^{+0.77}_{-0.57}$	$-12.12^{+0.39}_{-0.17}$	$4.7^{+0.3}_{-0.2}$ (21.3)	61.4/71
17 Nov 14	$2.2^{+2.9}_{-0.9}$	$0.74^{+0.09}_{-0.15}$	$0.06^{+0.04}_{-0.02}$	<-12.46	$-11.68^{+0.12}_{-0.16}$	$10.0^{+0.1}_{-0.3}$ (<16.6)	15.2/22
17 Dec 16	$3.5^{+3.0}_{-1.3}$	$0.58^{+0.16}_{-0.30}$	$0.13^{+0.06}_{-0.04}$	<-12.70	$-11.87^{+0.20}_{-0.22}$	$7.0^{+0.1}_{-0.3}$ (<13.6)	64.1/48
19 Dec 16	$6.1^{+7.9}_{-2.7}$	$0.81^{+0.05}_{-0.09}$	$0.08^{+0.04}_{-0.03}$	<-12.30	$-11.59^{+0.12}_{-0.16}$	$13.2^{+0.1}_{-0.4}$ (<18.2)	36.5/29
26 Apr 20	<5.1	0.73 ± 0.08	$0.10^{+0.41}_{-0.04}$	$-11.04^{+0.70}_{-2.44}$	$-11.66^{+0.12}_{-0.59}$	$54.8^{+0.35}_{-1.24}$ (79.7)	36.5/31
Average	$4.6^{+4.7}_{-2.5}$	$0.65^{+0.14}_{-0.18}$	$0.12^{+0.11}_{-0.04}$	<-12.43	$-11.81^{+0.28}_{-0.25}$	8.9 ± 0.2 (<16.7)	...

Note. L_{X} refers to the unabsorbed, 0.3–10 keV luminosity derived from the best-fit model.

et al. (2019) found

$$\log_{10} \text{EW}_{4686} = 0.97(\log_{10} \text{EW}_{1640}) + 0.58, \quad (2)$$

suggesting the ratio of the two EWs is near 3.8 (and roughly independent of stellar parameters) in Galactic and Large Magellanic Cloud (LMC) WN stars. The line fluxes are additionally found to be related to one another by

$$\log_{10} F_{4686} = (0.95 \pm 0.02)\log_{10} F_{1640} - (1.36 \pm 0.17). \quad (3)$$

We obtained FUV spectra of the WR donor star in the X-1 binary system that sample the binary orbital period with HST/COS. In this section, we present the analysis of these observations and compare them to the optical spectra (as a function of orbital phase) available in the literature (Crowther et al. 2010a).

5.1. UV Properties of the X-1 Donor Star

To infer the spectral properties of the donor star and compare them to those derived from optical observations, we first compare our UV spectra to the Potsdam Wolf-Rayet (PoWR; Todt et al. 2015) model atmospheres. Briefly, the PoWR models iteratively solve the (non-LTE) radiative transfer equation in the comoving frame of the expanding WR atmosphere (assuming spherical symmetry) simultaneously with the equations of both radiative and statistical equilibrium (Hamann & Gräfener 2004). The stellar radius R_* (defined as the radius at which $\tau_{\text{R}} = 20$), luminosity L_* , and temperature T_* are the main parameters of the model. Other relevant parameters are the stellar mass-loss rate \dot{M}_* and the terminal wind velocity v_∞ , which are combined into a quantity called

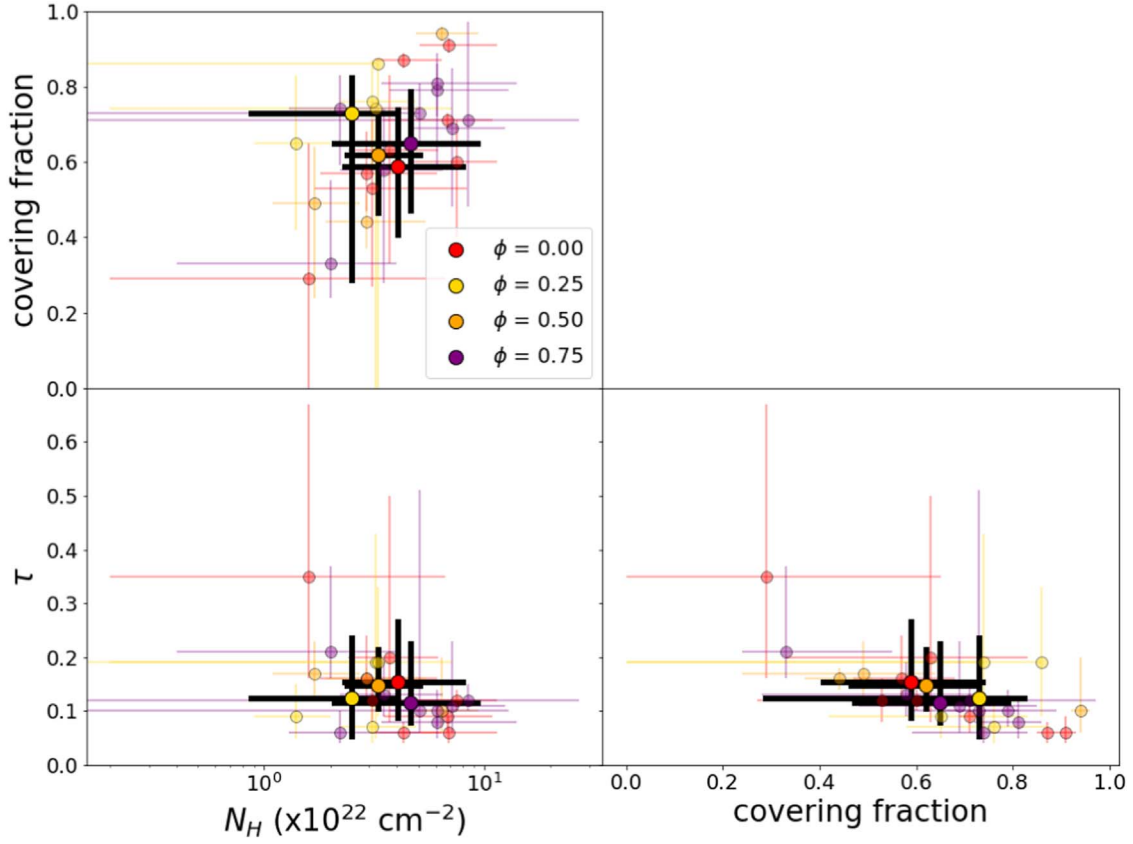


Figure 7. Comparison of N_H , partial covering fraction, and the Comptonizing plasma optical depth τ . Individual X-ray observations are color coded according to the corresponding orbital phases spanned by the HST observations. The average values are shown with thick, black error bars.

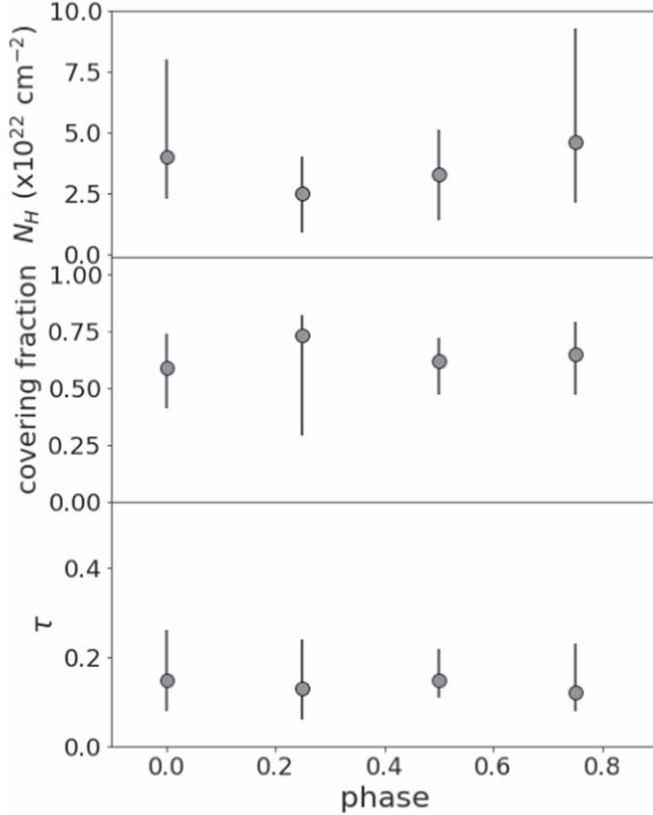


Figure 8. Average fit parameter values N_H (top), partial covering fraction (middle), and the optical depth τ (bottom) as a function of phase.

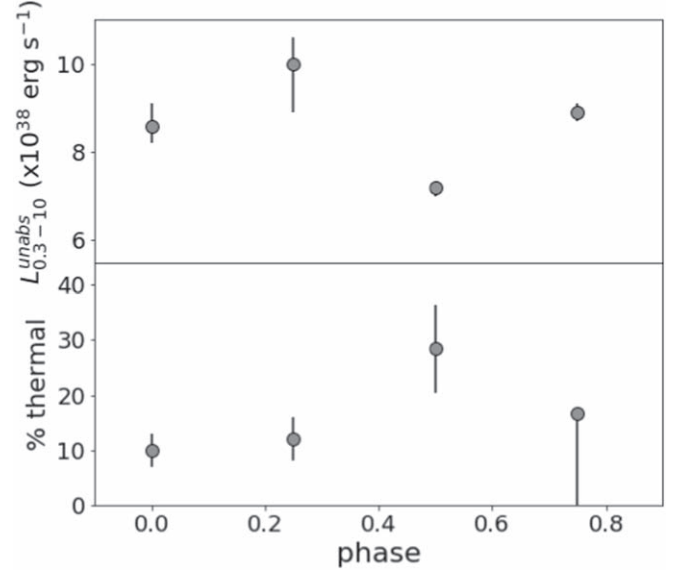


Figure 9. Average unabsorbed 0.3–10 keV L_X (top) and the fraction of the luminosity originating in the thermal component (bottom) as a function of phase.

the “transformed radius” R_t (Schmutz et al. 1989):

$$R_t = R_* \left[\left(\frac{v_\infty}{\dot{M} \sqrt{D}} \right) \left(\frac{10^{-4} M_\odot \text{ yr}^{-1}}{2500 \text{ km s}^{-1}} \right) \right]^{2/3}. \quad (4)$$

The quantity D is the clumping contrast, which parameterizes the inhomogeneities in the stellar wind. There is a significant

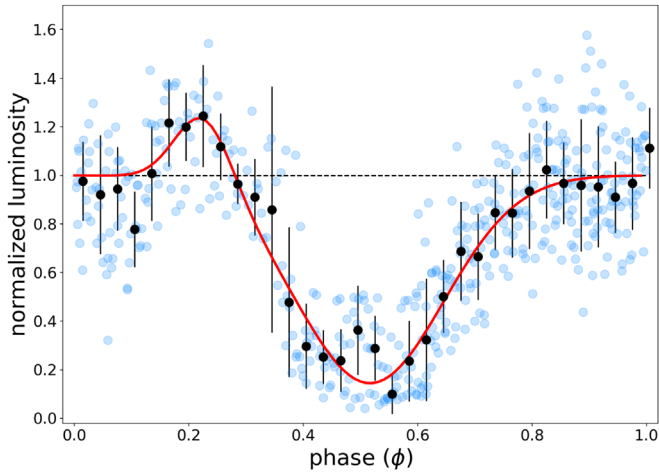


Figure 10. Reconstructed light curve with L_X derived from the best-fit spectral model for each observation and orbital phase, normalized to the average L_X from the $\phi = 0.75$ phase ($8.6 \times 10^{38} \text{ erg s}^{-1}$). The black points show the binned light curve. The red line shows a fit to the light curve with two Gaussian components: one representing the X-ray eclipse (centered at $\phi = 0.50$) and one showing the possible accretion stream impact on the disk edge at $\phi \sim 0.2$.

body of evidence supporting highly clumped winds in WR stars (Moffat et al. 1988; St.-Louis et al. 1993; Lépine et al. 2000; Kurosawa et al. 2002), and a value of $D = 10$ has been inferred for WN stars in the LMC (Crowther et al. 2010b; Doran et al. 2013). At higher (e.g., Galactic) metallicity, a value of $D = 4$ is more appropriate (Hamann & Koesterke 1998). Model spectra with equal values of R_t and T_* (and the same chemical composition) exhibit the same EWs of emission lines. Thus, although all PoWR model grids are computed assuming $\log(L/L_\odot) = 5.3$, the model parameters can be scaled to match an observed luminosity (i.e., $\dot{M}_* \propto L^{3/4}$) or to account for a different clumping contrast ($\dot{M}_* \propto D^{-1/2}$).

The spectrum obtained on 2020 April 29 corresponds to a binary orbital phase $\phi = 0.5$, when the WR star resides at inferior conjunction and the RV shifts due to the star’s orbital motion are expected to be minimal. The brightest emission line in that of H II $\lambda 1640$, while C IV $\lambda 1550$, N IV $\lambda 1718$, and N IV $\lambda 1486$ (which also contains emission features from Fe II) are also easily visible in the spectrum. We thus compare our observation to the PoWR models over a wavelength range of 1400–1750 Å and over three metallicity regimes: metallicities typical of the Milky Way, the LMC ($0.5Z_\odot$), and the Small Magellanic Cloud ($0.2Z_\odot$). In order to directly compare our observed spectrum to the PoWR models, we bin our observed spectrum to a resolution of 0.5 Å and interpolate the PoWR models to match the wavelength axis of our data. The model spectrum is then scaled to match the flux of the observed spectrum over the 1400–1750 Å wavelength range. We calculate the χ^2 value for each PoWR model compared to our observed spectrum, and models yielding $\chi^2 < 2$ (the “good” fits) are further inspected by eye.

Early-type, hydrogen-free (WNE) models at LMC metallicity were strongly preferred over late-type (WNL) models at Galactic or SMC metallicities. This result is consistent with the measured metallicity of NGC 300 at the location of the X-1 system (Urbaneja et al. 2005) and the optical spectrum, which also showed a lack of strong hydrogen features (Crowther et al. 2010a). We also tested LMC metallicity WC stellar models, but the weakness of the C IV $\lambda 1550$ line makes the WC designation

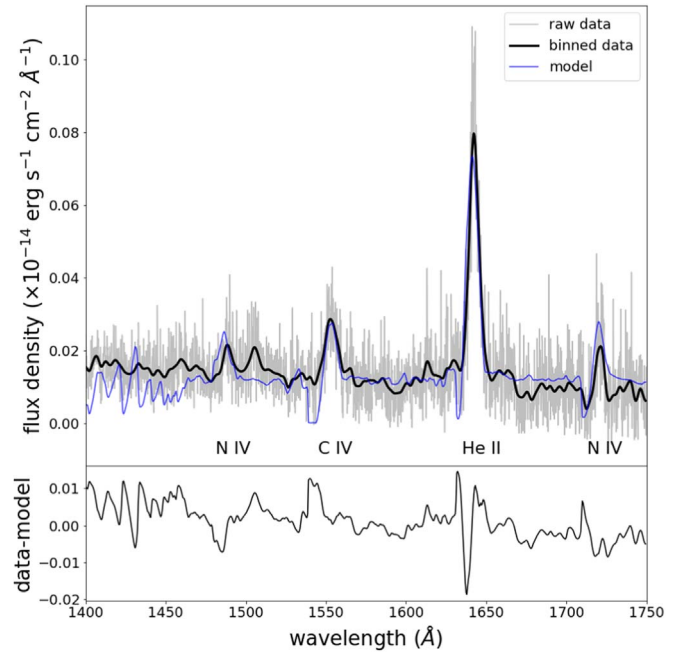


Figure 11. Top panel: best-fit PoWR models (blue) at LMC metallicity compared to the observed FUV spectrum (black line shows spectrum binned to 0.5 Å resolution, gray shows the unbinned data). The best-fit model has $T_* = 50\,100 \text{ K}$ and $R_t = 7.85 R_\odot$. Bottom panel: data-model residuals.

unlikely. Our observations therefore strongly support the WN designation of the donor star.

The best-fit PoWR model⁸ (which minimized the χ^2 value while yielding the smallest data-model residuals) is shown in Figure 11. It has an effective stellar temperature of 50,100 K. We scale the best-fit model to the observed optical luminosity found by Crowther et al. (2010a), which yields $R_t = 7.85 R_\odot$ and a mass-loss rate of $\dot{M}_* \sim 4 \times 10^{-5} M_\odot \text{ yr}^{-1}$. Thus, the UV spectrum is consistent with a somewhat cooler WR star than is suggested by the optical spectrum, although other models with higher values of T_* produce statistically acceptable fits to the data.

5.2. Specific Spectral Line Measurements

We next modeled the line profiles of specific UV lines using the Python packages `pyspeckit` (Ginsburg & Mirocha 2011) and `specutils`.⁹ In addition to the readily observable H II $\lambda 1640$, C IV $\lambda 1550$, N IV $\lambda 1718$, and N IV $\lambda 1486$ features, we also detect C II $\lambda 1334$ in absorption. For all spectral lines, we fit a Gaussian model (or a sum of multiple Gaussian components) to the data and the observed flux in each wavelength element is then randomly shifted to a value within the flux uncertainty of the observation, and the fit is performed again. This “bootstrapping” is performed 5000 times for each spectral line, and the 16th, 50th, and 84th percentiles of the resulting parameter distributions are used to derive the best-fit value and the 90% confidence interval of the parameters.

⁸ Best-fit model is available at <http://www.astro.physik.uni-potsdam.de/~wrh/PoWR/LMC-WNE/07-12>.

⁹ See <https://specutils.readthedocs.io/>.

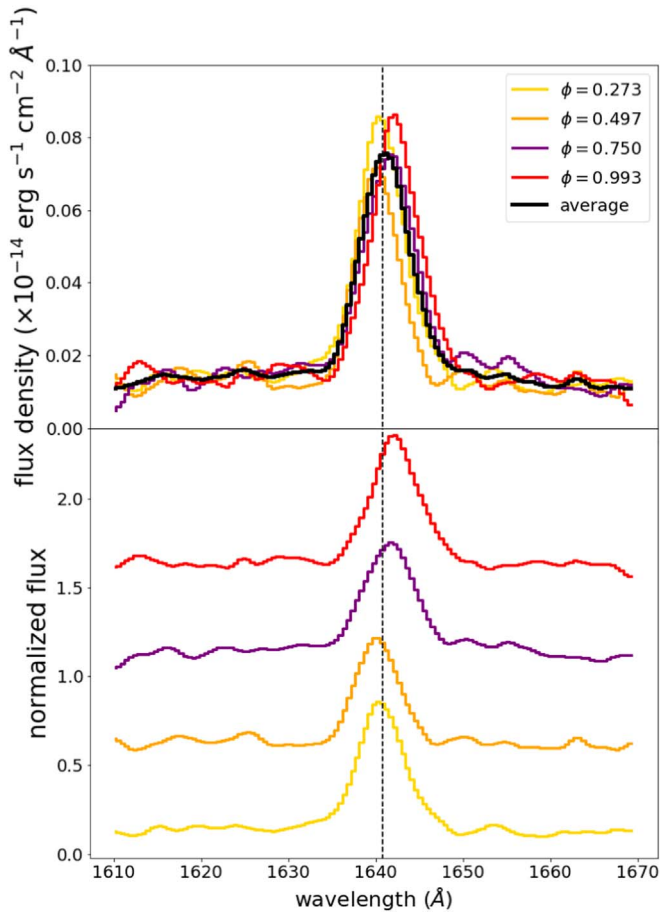


Figure 12. Top: the average He II $\lambda 1640$ emission line (black) compared to individual observations are shown (color coded according to orbital phase), showing a clear detection of the emission line. Spectra have been binned and smoothed for display purposes. Bottom: the He II $\lambda 1640$ emission line in each observation (normalized to the continuum level) with the best-fit Gaussian superimposed (the fluxes at each phase ϕ have an arbitrary offset applied for clarity). In both panels, the dashed line shows the rest-frame wavelength of He II $\lambda 1640$ corrected for the recessional velocity of NGC 300.

5.2.1. The H II $\lambda 1640$ Emission Line

H II $\lambda 1640$ is by far the strongest emission line present in the WR spectrum (see Figure 12). The best-fit parameters for the emission line are summarized in Table 4. In WR star winds, He II is excited collisionally and is a hallmark of the WN subtype. However, He II emission lines can also arise in the hot spots of compact object accretion disks (Crowley & Cramp-ton 1975; Steeghs & Casares 2002; Montgomery 2012) or colliding wind shocks (as has been studied extensively for η Car; Martin et al. 2006; Mehner et al. 2011; Teodoro et al. 2012; Madura et al. 2013; Teodoro et al. 2016), and thus the interpretation of this feature in a known HMXB requires some caution. In the optical, the He II $\lambda 4686$ EW is $\sim 56 \text{ \AA}^{10}$ and FWHM is $\sim 17 \text{ \AA}$, somewhat lower than observed in LMC and Milky Way WN stars (Crowther et al. 2010a). Given the observed correlation between the optical and UV EWs found by Leitherer et al. (2019), we therefore may expect the H II $\lambda 1640$ EW to be $\sim 15 \text{ \AA}$.

Instead, Table 4 reveals an emission line that exhibits strong variability with orbital phase. At $\phi = 0.497$, when the BH

accretion disk is largely eclipsed and we expect to view the WR winds with minimal X-ray irradiation, the H II $\lambda 1640$ EW is $\sim 25 \text{ \AA}$, and the FWHM and line fluxes are both at minimum values. This phase also corresponds to the strongest observed blueshift of the H II $\lambda 1640$ line (note that the RVs, RV_{cor} , listed in Table 4 have been corrected for the recessional velocity of NGC 300). Approximately half an orbital period later, at $\phi = 0.993$, we observe a strong redshift, a maximum line flux, and slightly larger values of the EW ($\sim 20\%$ larger than at $\phi = 0.497$) and FWHM ($\sim 30\%$ higher than at $\phi = 0.497$). The EW_{1640} is about twice the value predicted for single WN stars (Leitherer et al. 2019).

We use our updated ephemeris from Section 3 to recompute the phases at which the optical He II $\lambda 4686$ RVs from Crowther et al. (2010a) were obtained. We combine these with our H II $\lambda 1640$ measurements and fit a sinusoid to the data (we perform 500 iterations of the fit, randomly adjusting the RV measurements within the observed uncertainties, and again report the median and 90% confidence interval of the resulting fit parameter distributions). The results are shown in Figure 13. We measure the RV semi-amplitude K and the phase shift $\Delta\phi$ from the expected BH orbital motion. The results are summarized in Table 5. In addition to the combined UV + optical data set, we also fit the UV and optical measurements independently (our optical-only value of K is in excellent agreement with Crowther et al. 2010a).

There is a systematic phase delay of $\Delta\phi = 0.30$ observed in the He II RV data compared to the expected orbital motion of the BH. There is additionally marginal evidence (at approximately 2σ significance) for different values of K between the optical and UV data sets, with the UV observations showing a lower RV amplitude, suggesting that the two lines may be originating from slightly different locations in the X-1 system. When taken together, the observed phase delay and variable line profile indicate that bright He II emission (or at least a significant component of the line emission) is not originating uniformly in the WR wind but is instead arising from a more complex interaction between the two binary components. We discuss possible interpretations of the observed behavior in more detail in Section 6.

5.2.2. Fainter Emission Lines

The second strongest line detected in the HST/COS spectra is the UV resonance line C IV $\lambda 1550$ (shown in Figure 14, roughly a factor of 4 fainter than H II $\lambda 1640$ in flux), which is often used to estimate the v_∞ of WR stars. In addition to the emission peak at 1550 \AA , the P Cygni absorption component at 1548 \AA is typically seen in WR stars (and is present in the PoWR model). The depth and width of the C IV $\lambda 1550$ doublet are sensitive to the inclusion of X-ray radiation in the WR model atmosphere (Giménez-García et al. 2016). Although there are hints of a P Cygni line profile during phases 0.750 and 0.993, the signal-to-noise ratio is not sufficient for us to directly model multiple components; a single component Gaussian generally matches the largest flux value in amplitude, and the FWHM is calculated independently of the Gaussian model. Like H II $\lambda 1640$, C IV $\lambda 1550$ (see Table 6) is clearly complex and variable, with EW, FWHM, and line fluxes that vary as a function of orbital phase.

RV variations with orbital phase are also apparent in the line profile. The RV curve of C IV $\lambda 1550$ is shown in Figure 15. The general shape of the C IV $\lambda 1550$ RV curve matches the

¹⁰ Typically positive values of EW indicate an absorption line, however throughout this work we refer to EWs in terms of their absolute values.

Table 4
He II $\lambda 1640$ Line Measurements

Parameter (1)	Orbital Phase			
	0.273 (2)	0.497 (3)	0.750 (4)	0.993 (5)
λ_c (Å)	1640.89 ± 0.16	1640.42 ± 0.15	$1641.73^{+0.20}_{-0.19}$	$1642.73^{+0.17}_{-0.18}$
RV_{cor} (km s $^{-1}$)	-60 ± 30	-150 ± 30	90 ± 40	270 ± 30
EW (Å)	28.4 ± 1.2	$24.6^{+0.8}_{-0.9}$	$27.2^{+1.5}_{-1.4}$	29.8 ± 0.9
FWHM (Å)	6.14 ± 0.25	$4.65^{+0.15}_{-0.16}$	$5.95^{+0.33}_{-0.31}$	$5.93^{+0.17}_{-0.18}$
FWHM (km s $^{-1}$)	2245 ± 90	1700^{+55}_{-59}	2175^{+121}_{-113}	2170^{+62}_{-66}
F_{line} ($\times 10^{-15}$ erg s $^{-1}$ cm $^{-2}$)	4.67 ± 0.04	3.43 ± 0.03	4.14 ± 0.04	4.93 ± 0.04
$\log L_{\text{line}}$ (erg s $^{-1}$)	$36.35^{+0.03}_{-0.04}$	36.22 ± 0.04	$36.30^{+0.04}_{-0.05}$	36.37 ± 0.04

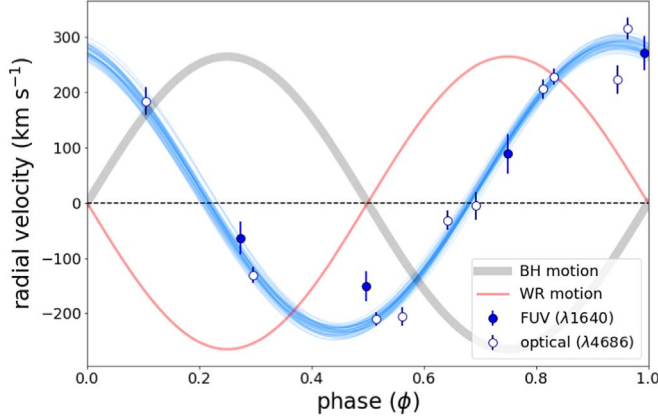


Figure 13. The RV curves for H II $\lambda 1640$ (solid blue circles) and He II $\lambda 4686$ (open circles, taken from Crowther et al. 2010a). The expected BH orbital motion (scaled to approximately match the amplitude of the He II curve) is shown for reference in gray, and the expected WR orbital motion is shown in red. The light blue lines show 50 random draws from our fits to the data.

Table 5
He II RV Curve Fit Parameters

Data Set (1)	K (km s $^{-1}$) (2)	$\Delta\phi$ (3)
UV + optical	260 ± 10	0.30 ± 0.01
UV only	220 ± 20	0.30 ± 0.02
Optical only	270 ± 10	0.30 ± 0.01

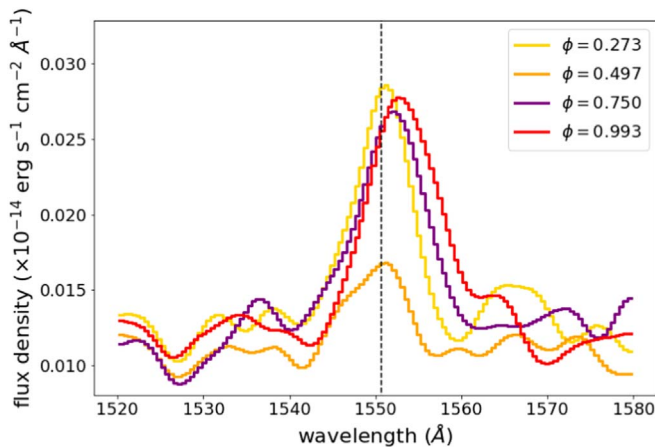


Figure 14. The C IV $\lambda 1550$ spectral feature line in each observation, smoothed for display purposes. The dashed line shows the rest-frame wavelength corrected for the recessional velocity of NGC 300.

expected orbital motion of the WR star. We assume the C IV $\lambda 1550$ RVs follow a sinusoidal curve (although with only four phase samples available, we cannot rigorously demonstrate that this is the case) and follow the same fitting procedure as for H II $\lambda 1640$. A systematic redshift of roughly 95 km s^{-1} is observed with a semi-amplitude $K = 250 \pm 40 \text{ km s}^{-1}$ and a phase offset consistent with zero ($\Delta\phi = 0.03 \pm 0.03$).

Other lines present in the WR spectrum are weaker still than C IV $\lambda 1550$. Their properties are summarized in Table 7. Given their low fluxes (an order of magnitude below C IV $\lambda 1550$) and complex line profiles (for example, N IV $\lambda 1486$ is a blend of several N IV and Fe V lines), we do not attempt to fully model these lines.

6. Discussion

The major results of our joint Chandra-HST program (supplemented with archival X-ray observations) include the pre-eclipse hump in the X-ray light curve, the phase delay in the optical and UV He II line RVs, and the RV variations observed in the C IV $\lambda 1550$ emission line. In this section, we discuss these results in more detail (including necessary assumptions and caveats) and present a model for the accretion flow in the X-1 binary system.

6.1. Binary Parameters and BH Mass

We can use the refined orbital period and C IV $\lambda 1550$ RV semi-amplitude (assuming the RV variations follow a sinusoidal curve) to estimate the binary parameters and ultimately constrain the mass of the X-1 BH. Crowther et al. (2010a) constrained the inclination of the X-1 system to $i = 60\text{--}75^\circ$, and our light curve (Figure 10) is consistent with these values.

In Section 5.2.2, we discovered the RV of the C IV $\lambda 1550$ emission line feature closely tracks the expected orbital motion of the WR star, with a semi-amplitude $K = 250 \pm 40 \text{ km s}^{-1}$. This measurement allows us to derive an updated mass estimate of the BH:

$$M_{\text{BH}} = \frac{PK^3}{2\pi G} \frac{(1+q)^2}{\sin^3 i} \quad (5)$$

where q is the mass ratio between the donor star (M_*) and the compact object ($q = M_*/M_{\text{BH}}$). We assume the preferred $M_* = 26 M_\odot$ from Crowther et al. (2010a) and use our measurements of the orbital period ($P = 32.7921 \text{ hr}$) and K from the C IV line. For inclination angles ranging from $60\text{--}75^\circ$, we derive $M_{\text{BH}} = 17 \pm 4 M_\odot$. This is somewhat lower than the original estimate of $\sim 20 M_\odot$. If we assume $M_* = 15 M_\odot$, which

Table 6
C IV $\lambda 1550$ Line Measurements

Parameter (1)	Orbital Phase			
	0.273 (2)	0.497 (3)	0.750 (4)	0.993 (5)
λ_c (Å)	1551.00 ± 0.08	1551.44 ± 0.04	$1553.56^{+0.08}_{-0.32}$	1551.96 ± 0.08
RV_{cor} (km s $^{-1}$)	-100 ± 30	-10 ± 20	400^{+30}_{-60}	90 ± 30
EW (Å)	10.0 ± 0.1	$5.3^{+0.6}_{-0.7}$	$9.8^{+0.9}_{-0.8}$	13.9 ± 0.1
FWHM (Å)	2.8 ± 0.5	1.9 ± 0.1	6.3 ± 0.1	6.1 ± 0.1
F_{line} ($\times 10^{-15}$ erg s $^{-1}$ cm $^{-2}$)	1.15 ± 0.01	0.46 ± 0.01	1.25 ± 0.01	1.44 ± 0.01

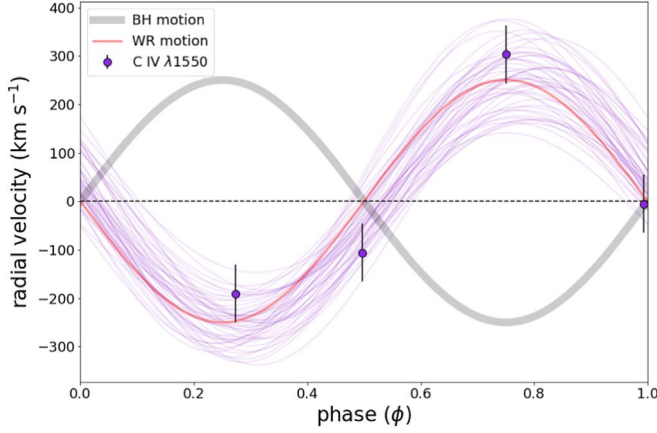


Figure 15. Same as Figure 13, but for C IV $\lambda 1550$.

Table 7
Properties of Other Faint Spectral Lines

line ID (1)	Orbital Phase (2)	λ_c (Å) (3)	FWHM (Å) (4)	EW (Å) (5)	F_{line}^a (erg s $^{-1}$ cm $^{-2}$) (6)
C II $\lambda 1334$	0.273	1335.08	1.4	-1.2	...
	0.497	1334.84	2.0	-1.0	...
	0.750	1334.84	2.2	-0.5	...
	0.993	1335.08	1.6	-1.0	...
N IV $\lambda 1468$	0.273	1486.86	5.8	6.0	7.2×10^{-16}
	0.497	1484.48	6.2	5.2	5.9×10^{-16}
	0.750	1486.13	4.8	2.9	3.9×10^{-16}
	0.993	1488.30	5.1	1.4	1.3×10^{-16}
N IV $\lambda 1718$	0.273	1718.15	5.7	3.7	4.8×10^{-16}
	0.497	1721.03	7.7	11.2	5.4×10^{-16}
	0.750	1720.06	5.6	5.4	6.0×10^{-16}
	0.993	1721.50	5.6	5.8	5.5×10^{-16}

Note.

^a Fluxes are not reported for absorption lines, and we adopt a convention where the absorption line EWs are negative.

is also consistent with the Crowther et al. (2010a) results (and is a typical value of WN stars in the Milky Way), the BH mass is reduced to $13 M_{\odot}$.

Using our new estimate of $M_{\text{BH}} = 17 M_{\odot}$, we can now utilize Kepler's third law to solve for the orbital separation a :

$$a = \left[\frac{G(M_{\text{BH}} + M_{\star})}{4\pi^2} P^2 \right]^{1/3} \quad (6)$$

and estimate the size of the WR Roche lobe (Eggleton 1983):

$$r_L = \left[\frac{0.49q^{2/3}}{0.6q^{2/3} + \ln(1 + q^{1/3})} \right] a. \quad (7)$$

We find an orbital separation $a = 18.2^{+0.5}_{-0.6} R_{\odot}$ and $r_L = 7.6 R_{\odot}$ (implying an orbital speed of ~ 670 km s $^{-1}$). Assuming a $R_{\star} = 7.2 R_{\odot}$, we estimate $R_{\star}/a = 0.4$ and $R_{\star}/r_L = 0.95$. If we instead assume a lower-mass system (with $M_{\star} = 15 M_{\odot}$, $R_{\star} = 4.8 R_{\odot}$, and $M_{\text{BH}} = 12 M_{\odot}$), we find $a = 15.8 R_{\odot}$ and $r_L = 6.2 R_{\odot}$, implying $R_{\star}/a = 0.3$ and $R_{\star}/r_L = 0.77$. Thus, the WR star does not completely fill its Roche lobe, making it unlikely that the standard model of Roche lobe overflow (RLOF) is occurring in the X-1 system.

6.2. The Mass Accretion Geometry

Without standard RLOF, mass transfer in the NGC 300 X-1 system must occur through gravitational interactions between the BH and the WR winds via a process similar to Bondi–Hölye–Lyttleton wind accretion (Bondi & Hoyle 1944; Edgar 2004). This standard model of direct wind accretion typically yields X-ray luminosities much lower than those observed in X-1 (by ~ 2 – 3 orders of magnitude; see also Martínez-Núñez et al. 2017 and references therein). More recent simulations of wind-capture disks (Huarte-Espinosa et al. 2013) and wind RLOF (El Mellah et al. 2019a, 2019b), however, provide a mechanism by which a compact object may form an accretion disk with a mass accretion rate sufficient to maintain the high L_X without the need for standard RLOF from the donor star (the relevant Roche lobe in the wind-RLOF scenario is that of the *compact object*, not of the donor star). Indeed, Tutukov & Fedorova (2016) invoked such an explanation to reconcile the high \dot{M}_{\star} values of WR donors and the observed L_X of both NGC 300 X-1 and IC 10 X-1.

When the winds of the donor star are slow relative to the orbital motion of the compact object, the gravitational influence of the compact object can strongly beam the wind toward the accretor. Such a scenario has been explored for symbiotic binaries (Podsiadlowski & Mohamed 2007), and its application to ultraluminous sources (ULXs) and supergiant XRBs is an active area of study (Huarte-Espinosa et al. 2013; El Mellah et al. 2019a, 2019b). The terminal speeds of WR winds can be slowed considerably when irradiated by a strong X-ray source (Hatchett & McCray 1977; Fransson & Fabian 1980; Giménez-García et al. 2016). This ionization of the wind is expected to occur even for relatively large separations between the donor star and the X-ray source (Blondin et al. 1991; Manousakis & Walter 2015). This beamed, slowly moving wind material does not directly accrete onto the compact object but forms a

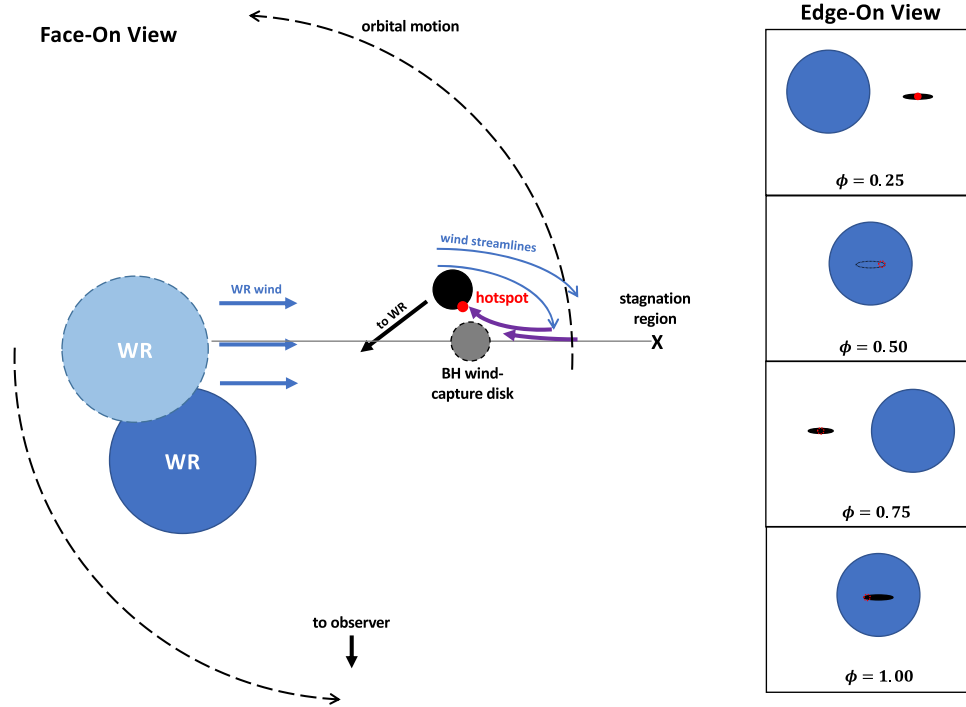


Figure 16. Toy model of the X-1 geometry, not to scale. The left side of the figure presents a face-on view of the system. The WR star is shown in blue, and the blue arrows indicate the flow of the WR winds. The black circle indicates the BH accretion disk. The lighter, dashed-outline circles show the prior locations of the binary components due to their orbital motion. The purple arrows indicate the formation of the accretion stream, which then impacts the BH disk and generates a hot spot (red). The right side of the figure shows the edge-on view of the system. Filled shapes indicate a component is visible to the observer; dotted outlines indicate the structure is largely or entirely obscured from the observer’s line of sight. Observations of X-1 imply a inclination of $i = 60\text{--}75^\circ$.

downstream wake and flows into an accretion stream as shown in Figure 1 of Huarte-Espinosa et al. (2013) or Figure 4 of El Mellah et al. (2019a). Due to the orbital motion of the binary components, the focused wind material is accelerated toward the earlier position of the accretor, and so the final impact of material flowing through the accretion stream and the accretion disk does not occur on the portion of the disk facing the donor star.

Not only does this model reproduce the X-ray luminosities observed in X-1, it also provides a natural mechanism by which a hot spot on the accretion disk can form at $\phi \sim 0.2$. In Figure 16, we present a “cartoon model” of the X-1 system inspired by the hydrodynamical simulations of El Mellah et al. (2019a, 2019b) and Huarte-Espinosa et al. (2013) that illustrates how the wind-capture model may give rise to an accretion disk with a hot spot consistent with our observations. The WR star is shown in blue, with blue arrows indicating the flow of the WR winds (not to scale). The BH accretion disk is shown in black. The purple arrows show the formation of the accretion stream, which impacts the disk and generates a hot spot (red). When viewed edge-on, the hot spot is visible to an observer at phases $\phi \sim 0.25$. Neither the BH accretion disk nor the hot spot is visible during the eclipse ($\phi = 0.5$), and when the accretion disk is visible at phases $\phi \sim 0.75\text{--}1.0$, the hot spot is on the side of the accretion disk opposite to the observer.

There is an apparent dichotomy observed among stellar mass BHs in XRBs: wind-fed BHs (notably Cyg X-1, LMC X-1, and M33 X-7) exhibit systematically higher masses and higher BH spins compared to BHs fed via RLOF (Özel et al. 2010; McClintock et al. 2014; Steiner et al. 2014; Fragos & McClintock 2015). This dichotomy has been attributed to the age of the system: BHs in wind-fed systems contain massive companions and therefore must be young, while the majority of

BHs undergoing RLOF are observed in low-mass XRBs and are thus likely to be much older. The emerging picture of NGC 300 X-1 as a high-mass stellar BH powered via a wind-captured disk is thus consistent with observations of other comparable systems.

6.3. The Origin of the He II and C IV Emission Lines

The model described above, with a wind-captured accretion disk being impacted by an accretion stream originating in an X-ray irradiated wind, can additionally be used to interpret the prominent emission lines discussed in Section 5: H II $\lambda 1640$ (and He II $\lambda 4686$ from the literature) and C IV $\lambda 1550$.

The changes in the H II $\lambda 1640$ line luminosity are perhaps the least surprising: if a significant portion of the accretion disk is being eclipsed by the WR star at $\phi = 0.5$, we expect the UV emission to be similarly diminished. Indeed, this is what we observe, with the line luminosity increasing to a maximum value at phases $\sim 0\text{--}0.25$, presumably as the accretion disk and impact site hot spot are rotating back into the full view of the observer. The inclination of the system is not perfectly edge-on, as depicted in Figure 16, so we would not expect the accretion disk’s contribution to the UV emission to vanish (just as the X-ray emission does not vanish at $\phi = 0.5$). Furthermore, both the UV and optical He II emission lines could be formed in shocked regions within the accretion stream, which can have a significant physical extent orthogonal to the plane of the accretion disk (El Mellah et al. 2019a). Because the accretion stream itself can have a large physical extent from the BH accretion disk (both in the plane of the binary as well as orthogonal to the orbital plane), the phase lag observed in the He II may indicate that these lines form in a hot, dense portion of the accretion stream that lags the BH.

A similar decrease in both line luminosity and EW at $\phi = 0.5$ are also seen in the C IV $\lambda 1550$ line despite the RV variations that coincide very strongly with the expected motion of the WR star's orbital motion. The fact that the C IV $\lambda 1550$ line flux varies with orbital phase (specifically, the decline in the line flux near $\phi = 0.5$) suggests that there is an asymmetric component to the line flux. This is likely due to X-ray irradiation of the wind by the BH accretion disk: X-ray irradiation significantly enhances the C IV population in the wind (as in Vela X-1; Giménez-García et al. 2016) and decreases the terminal velocity of the irradiated wind (Hatchett & McCray 1977; Fransson & Fabian 1980). As a resonance line, the blue C IV $\lambda 1548$ line experiences a larger optical depth to resonant scattering than the red $\lambda 1550$ line (with relative oscillator strengths of $f_{1548}/f_{1550} \sim 2$). As the optical depth increases, the 1548 Å photons are scattered out of the line of sight. Given that no strong feature was detected blueward of the 1550 Å emission line, we can infer that the C IV $\lambda 1550$ emission line originates in an optically thick portion of the WR wind, where it is excited primarily via collisions. Therefore, during the eclipse we are likely seeing only the C IV $\lambda 1550$ emission originating in the portion of the WR wind that is “shadowed” from the X-rays, while at other orbital phases we can observe the contribution from C IV $\lambda 1550$ emission originating in the photoionized portion of the WR wind. As recombination lines, the optical and UV He II lines form predominantly in the lower density, lower optical depth regions of the X-1 system—such as the accretion stream and BH accretion disk hot spot.

In using the C IV $\lambda 1550$ emission line to trace the RV of the donor star, we have assumed that the emission-weighted mean line velocity is the same as the center of mass velocity of the WR star. This assumption may not be valid if significant asymmetries exist in the C IV $\lambda 1550$ line as a function of phase or if the terminal speed of the WR wind varies in different directions due to the X-ray irradiation from the BH accretion disk. Similar issues are discussed in detail in Koljonen & Maccarone (2017), where phase-resolved optical and IR spectroscopy of Cyg X-3 was analyzed. To fully evaluate the extent to which these assumptions affect our BH mass estimate would require a significantly larger investment of HST observing time or more detailed theoretical modeling of the WR wind structure, which is beyond the scope of this work. Comparing NGC 300 X-1 to other similar systems (e.g., such as Cyg X-3 or IC 10 X-1) can also aid in resolving these issues.

7. Summary

We have presented an analysis of new Chandra/ACIS-I and HST/COS observations of the WR + BH binary NGC 300 X-1. The combination of our new Chandra exposure with nearly two decades of archival X-ray observations with Chandra and XMM-Newton have yielded a highly precise value of the binary orbital period: 32.7921 ± 0.0003 hr. Phase-resolved X-ray spectroscopy indicates that the underlying X-ray continuum of X-1 remains constant throughout the binary's orbital period with the unabsorbed X-ray luminosity decreasing during a partial eclipse by the WR star. We find that $\sim 70\%$ of L_X originated from a Comptonizing component, likely associated with the BH and its accretion disk, with the remainder originating in a soft, thermal component that may be due to shocks both within the WR winds or the collision between the WR winds and BH accretion disk winds. The

X-ray light curve shows evidence of a pre-eclipse hump, which we interpret as an accretion stream impacting the edge of the BH accretion disk (analogous to the accretion streams seen in the UV light curves of some CVs).

The UV spectrum is generally consistent with models of WN stars (at LMC metallicity) from the PoWR simulations with $T_\star \sim 50$ kK and a mass-loss rate of $\dot{M}_\star \sim 4 \times 10^{-5} M_\odot \text{ yr}^{-1}$. The brightest emission line in the UV spectrum belongs to H II $\lambda 1640$, which shows distinct RV variations over the binary orbital period. However, these RV shifts exhibit a systematic offset from the predicted motion of the binary components. Just as with the optical He II $\lambda 4686$ emission lines, H II $\lambda 1640$ lags the expected BH motion by $\Delta\phi = 0.30$. The EW is also larger than anticipated for a WN stars, indicating that these He II emission lines are primarily originating from the nonstellar component of the system. C IV $\lambda 1550$ is found to closely track the expected WR orbital motion. Assuming the C IV $\lambda 1550$ RV variations follow a sinusoidal curve, we measure an RV semi-amplitude of $250 \pm 40 \text{ km s}^{-1}$, implying a BH mass of $M_{\text{BH}} = 17 \pm 4 M_\odot$ (assuming a WR mass of $26 M_\odot$) and an orbital separation of $\sim 18.2 R_\odot$ between the WR and BH.

The derived binary parameters indicate that the WR star does not completely fill its Roche lobe. We therefore favor a wind-captured accretion disk scenario, where material from the WR winds is gravitationally focused into a thin disk around the BH. Under this model, wind material is funneled into an accretion stream that may be significantly misaligned with the orbital motion (and orbital plane) of the system, explaining the observed phase lags in the He II emission lines and the existence of a hot spot where the accretion stream impacts the edge of the disk.





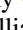

We thank the anonymous reviewer for comments and suggestions that improved this manuscript. Support for this work was provided by the National Aeronautics and Space Administration through Chandra Award Number GO0-21031X issued by the Chandra X-ray Observatory Center, which is operated by the Smithsonian Astrophysical Observatory for and on behalf of the National Aeronautics Space Administration under contract NAS8-03060. D.M.C. and S.L. acknowledge support from the NASA Astrophysics Data Analysis Program grant 80NSSC18K0430. This research has made use of data obtained from the Chandra Data Archive and software provided by the Chandra X-ray Center (CXC) in the application package CIAO. This research is based on observations made with the NASA/ESA HST obtained from the Space Telescope Science Institute, which is operated by the Association of Universities for Research in Astronomy, Inc., under NASA contract NAS 526555. These observations are associated with program 15999. This work is based on observations obtained with XMM-Newton, an ESA science mission with instruments and contributions directly funded by ESA Member States and NASA. This research made use of Astropy, a community-developed core Python package for Astronomy (Astropy Collaboration et al. 2013, 2018).

Facilities: HST/COS, CXO, XMM-Newton.

Software: astropy (Astropy Collaboration et al. 2013, 2018), pyspeckit (Ginsburg & Mirocha 2011), CIAO (Fruscione et al. 2006).

ORCID iDs

Breanna A. Binder  <https://orcid.org/0000-0002-4955-0471>

Michael Eracleous  <https://orcid.org/0000-0002-3719-940X>
 Dimitris M. Christodoulou  <https://orcid.org/0000-0002-7652-2206>
 Rigel Cappallo  <https://orcid.org/0000-0003-0267-8432>
 Silas Laycock  <https://orcid.org/0000-0002-8427-0766>
 Paul P. Plucinsky  <https://orcid.org/0000-0003-1415-5823>
 Benjamin F. Williams  <https://orcid.org/0000-0002-7502-0597>

References

- Aftab, N., Paul, B., & Kretschmar, P. 2019, *ApJS*, **243**, 29
- Arnaud, K. A. 1996, in ASP Conf. Ser. 101, *Astronomical Data Analysis Software and Systems V*, ed. G. H. Jacoby & J. Barnes (San Francisco, CA: ASP), 17
- Astropy Collaboration, Price-Whelan, A. M., SipHocz, B. M., et al. 2018, *AJ*, **156**, 123
- Astropy Collaboration, Robitaille, T. P., Tollerud, E. J., et al. 2013, *A&A*, **558**, A33
- Barnard, R., Clark, J. S., & Kolb, U. C. 2008, *A&A*, **488**, 697
- Binder, B., Gross, J., Williams, B. F., & Simons, D. 2015, *MNRAS*, **451**, 4471
- Binder, B., Williams, B. F., Eracleous, M., et al. 2011, *ApJ*, **742**, 128
- Binder, B., Williams, B. F., Eracleous, M., et al. 2012, *ApJ*, **758**, 15
- Blondin, J. M. 1994, *ApJ*, **435**, 756
- Blondin, J. M., Kallman, T. R., Fryxell, B. A., & Taam, R. E. 1990, *ApJ*, **356**, 591
- Blondin, J. M., Stevens, I. R., & Kallman, T. R. 1991, *ApJ*, **371**, 684
- Bondi, H., & Hoyle, F. 1944, *MNRAS*, **104**, 273
- Carpano, S., Haberl, F., Crowther, P., & Pollock, A. 2019, in Proc. IAU Symp. **346**, 187
- Carpano, S., Haberl, F., Maitra, C., & Vasilopoulos, G. 2018, *MNRAS*, **476**, L45
- Carpano, S., Pollock, A. M. T., Prestwich, A., et al. 2007, *A&A*, **466**, L17
- Castor, J. I., Abbott, D. C., & Klein, R. I. 1975, *ApJ*, **195**, 157
- Conti, P. S., & Morris, P. W. 1990, *AJ*, **99**, 898
- Cowley, A. P., & Crampton, D. 1975, *ApJL*, **201**, L65
- Crowther, P. A. 2007, *ARA&A*, **45**, 177
- Crowther, P. A., Barnard, R., Carpano, S., et al. 2010a, *MNRAS*, **403**, L41
- Crowther, P. A., Carpano, S., Hadfield, L. J., & Pollock, A. M. T. 2007, *A&A*, **469**, L31
- Crowther, P. A., Schnurr, O., Hirschi, R., et al. 2010b, *MNRAS*, **408**, 731
- Dalcanton, J. J., Williams, B. F., Seth, A. C., et al. 2009, *ApJS*, **183**, 67
- Day, C. S. R., & Stevens, I. R. 1993, *ApJ*, **403**, 322
- de Jong, J. A., van Paradijs, J., & Auguestijn, T. 1996, *A&A*, **314**, 484
- Doran, E. I., Crowther, P. A., de Koter, A., et al. 2013, *A&A*, **558**, A134
- Earnshaw, H. M., & Roberts, T. P. 2017, *MNRAS*, **467**, 2690
- Edgar, R. 2004, *NewAR*, **48**, 843
- Eggleton, P. P. 1983, *ApJ*, **268**, 368
- El Mellah, I., Sander, A. A. C., Sundqvist, J. O., & Keppens, R. 2019a, *A&A*, **622**, A189
- El Mellah, I., Sundqvist, J. O., & Keppens, R. 2019b, *A&A*, **622**, L3
- Fragos, T., & McClintock, J. E. 2015, *ApJ*, **800**, 17
- Fransson, C., & Fabian, A. C. 1980, *A&A*, **87**, 102
- Fruscione, A., McDowell, J. C., Allen, G. E., et al. 2006, *Proc. SPIE*, **6270**, 62701V
- Gehrels, N. 1986, *ApJ*, **303**, 336
- Gierliński, M., Done, C., & Page, K. 2009, *MNRAS*, **392**, 1106
- Giménez-García, A., Shenar, T., Torrejón, J. M., et al. 2016, *A&A*, **591**, A26
- Ginsburg, A., & Mirocha, J. 2011, PySpecKit: Python Spectroscopic Toolkit v0.1.22 ascl:1109.001
- Hamann, W. R., & Gräfener, G. 2004, *A&A*, **427**, 697
- Hamann, W. R., Gräfener, G., & Liermann, A. 2006, *A&A*, **457**, 1015
- Hamann, W. R., & Koesterke, L. 1998, *A&A*, **335**, 1003
- Hatchett, S., & McCray, R. 1977, *ApJ*, **211**, 552
- HI4PI Collaboration, Ben Bekhti, N., Flöer, L., et al. 2016, *A&A*, **594**, A116
- Hoard, D. W., Lu, T.-N., Knigge, C., et al. 2010, *AJ*, **140**, 1313
- Huarte-Espinosa, M., Carroll-Nellenback, J., Nordhaus, J., Frank, A., & Blackman, E. G. 2013, *MNRAS*, **433**, 295
- Kaper, L., Hammerschlag-Hensberge, G., & Zuiderwijk, E. J. 1994, *A&A*, **289**, 846
- Koliopanos, F., Vasilopoulos, G., Buchner, J., Maitra, C., & Haberl, F. 2019, *A&A*, **621**, A118
- Koljonen, K. I. I., & Maccarone, T. J. 2017, *MNRAS*, **472**, 2181
- Krtićka, J., Kubát, J., & Krtićková, I. 2015, *A&A*, **579**, A111
- Kurosawa, R., Hillier, D. J., & Pittard, J. M. 2002, *A&A*, **388**, 957
- Lauberts, A., & Valentijn, E. A. 1989, *Msngr*, **56**, 31
- Laycock, S. G. T., Cappallo, R. C., & Moro, M. J. 2015a, *MNRAS*, **446**, 1399
- Laycock, S. G. T., Maccarone, T. J., & Christodoulou, D. M. 2015b, *MNRAS*, **452**, L31
- Leitherer, C., Lee, J. C., & Faisst, A. 2019, *AJ*, **158**, 192
- Lépine, S., Moffat, A. F. J., St-Louis, N., et al. 2000, *AJ*, **120**, 3201
- Lucy, L. B., & Solomon, P. M. 1970, *ApJ*, **159**, 879
- Madura, T. I., Gull, T. R., Okazaki, A. T., et al. 2013, *MNRAS*, **436**, 3820
- Manousakis, A., & Walter, R. 2015, *A&A*, **584**, A25
- Marchenko, S. V., Moffat, A. F. J., Crowther, P. A., et al. 2004, *MNRAS*, **353**, 153
- Marsh, T. R., & Horne, K. 1990, *ApJ*, **349**, 593
- Marsh, T. R., Horne, K., Schlegel, E. M., Honeycutt, R. K., & Kaitchuck, R. H. 1990, *ApJ*, **364**, 637
- Martin, J. C., Davidson, K., Humphreys, R. M., Hillier, D. J., & Ishibashi, K. 2006, *ApJ*, **640**, 474
- Martínez-Núñez, S., Kretschmar, P., Bozzo, E., et al. 2017, *SSRv*, **212**, 59
- McClintock, J. E., Narayan, R., & Steiner, J. F. 2014, *SSRv*, **183**, 295
- Mehner, A., Davidson, K., Martin, J. C., et al. 2011, *ApJ*, **740**, 80
- Moffat, A. F. J., Drissen, L., Lamontagne, R., & Robert, C. 1988, *ApJ*, **334**, 1038
- Montgomery, M. M. 2012, *ApJL*, **745**, L25
- Özel, F., Psaltis, D., Narayan, R., & McClintock, J. E. 2010, *ApJ*, **725**, 1918
- Podsiadlowski, P., & Mohamed, S. 2007, *BaltA*, **16**, 26
- Prestwich, A. H., Kilgard, R., Crowther, P. A., et al. 2007, *ApJL*, **669**, L21
- Rutten, R. G. M., van Paradijs, J., & Tinbergen, J. 1992, *A&A*, **260**, 213
- Schmutz, W., Hamann, W. R., & Wessolowski, U. 1989, *A&A*, **210**, 236
- Schulz, N. S., Canizares, C. R., Lee, J. C., & Sako, M. 2002, *ApJL*, **564**, L21
- Silverman, J. M., & Filippenko, A. V. 2008, *ApJL*, **678**, L17
- Stanishev, V., Kraicheva, Z., Boffin, H. M. J., et al. 2004, *A&A*, **416**, 1057
- Steehls, D., & Casares, J. 2002, *ApJ*, **568**, 273
- Steiner, J. F., McClintock, J. E., Orosz, J. A., et al. 2014, *ApJL*, **793**, L29
- St-Louis, N., Howarth, I. D., Willis, A. J., et al. 1993, *A&A*, **267**, 447
- Suleimanov, V., Meyer, F., & Meyer-Hofmeister, E. 2003, *A&A*, **401**, 1009
- Teodoro, M., Damineli, A., Arias, J. I., et al. 2012, *ApJ*, **746**, 73
- Teodoro, M., Damineli, A., Heathcote, B., et al. 2016, *ApJ*, **819**, 131
- Todt, H., Sander, A., Hainich, R., et al. 2015, *A&A*, **579**, A75
- Tutukov, A. V., & Fedorova, A. V. 2016, *ARep*, **60**, 106
- Urbaneja, M. A., Herrero, A., Bresolin, F., et al. 2005, *ApJ*, **622**, 862
- van Kerkwijk, M. H. 1993, *A&A*, **276**, L9
- Walton, D. J., Bachetti, M., Fürst, F., et al. 2018, *ApJL*, **857**, L3
- Wolf, C. J. E., & Rayet, G. 1867, *CRAS*, **65**, 292